Monthly Notices of the ROYAL ASTRONOMICAL SOCIETY

MNRAS **448,** 3132–3155 (2015) doi:10.1093/mnras/stu2700

The binary fraction of planetary nebula central stars – II. A larger sample and improved technique for the infrared excess search

Dimitri Douchin,[1,2,3⋆] Orsola De Marco,[1,2] D. J. Frew,[1,2] G. H. Jacoby,[4] G. Jasniewicz,[3] M. Fitzgerald,[1,2] Jean-Claude Passy,[5] D. Harmer,[6] Todd Hillwig[7] and Maxwell Moe[8]

[1]Department of Physics and Astronomy, Macquarie University, Sydney, NSW 2109, Australia
[2]Astronomy, Astrophysics and Astrophotonics Research Centre, Macquarie University, Sydney, NSW 2109, Australia
[3]Laboratoire Univers et Particules, Université Montpellier 2, F-34095 Montpellier Cedex 5, France
[4]Giant Magellan Telescope and Carnegie Observatories, Pasadena, CA 91101, USA
[5]Department of Physics and Astronomy, University of Victoria, Victoria, BC V8P5C2, Canada
[6]Kitt Peak National Observatory, NOAO, PO Box 26732, Tucson, AZ 85719, USA
[7]Department of Physics and Astronomy, Valparaiso University, Valparaiso, IN 46383, USA
[8]Harvard–Smithsonian Center for Astrophysics, Cambridge, MA 02138, USA

Accepted 2014 December 18. Received 2014 December 17; in original form 2014 May 28

ABSTRACT

There is no conclusive explanation of why ∼80 per cent of planetary nebulae (PNe) are non-spherical. In the Binary Hypothesis, a binary interaction is a preferred channel to form a non-spherical PN. A fundamental step to corroborate or disprove the Binary Hypothesis is to estimate the binary fraction of central stars of PNe (CSPNe) and compare it with a prediction based on the binary fraction of the progenitor, main-sequence population. In this paper, the second in a series, we search for spatially unresolved I- and J-band flux excess in an extended sample of 34 CSPN by a refined measurement technique with a better quantification of the uncertainties. The detection rate of I- (J-)band flux excess is 32 ± 16 per cent (50 ± 24 per cent). This result is very close to what was obtained in Paper I with a smaller sample. We account conservatively for unobserved cool companions down to brown dwarf luminosities, increasing these fractions to 40 ± 20 per cent (62 ± 30 per cent). This step is very sensitive to the adopted brightness limit of our survey. Accounting for visual companions increases the binary fraction to 46 ± 23 per cent (71 ± 34 per cent). These figures are lower than in Paper I. The error bars are better quantified, but still unacceptably large. Taken at face value, the current CSPN binary fraction is in line with the main-sequence progenitor population binary fraction. However, including white dwarfs companions could increase this fraction by as much as 13 (21) per cent points.

Key words: techniques: photometric – surveys – binaries: general – stars: evolution – stars: statistics – planetary nebulae: general.

1 INTRODUCTION

It is not understood yet why a high 80 per cent of planetary nebulae (PNe) are non-spherical (Parker et al. 2006). The Binary Hypothesis – the paradigm in which PNe are preferentially produced by a binary interaction (De Marco 2009) – may enable us to explain such figures. A first important step to test the Binary Hypothesis is to estimate the binary fraction of central stars of PNe (CSPNe) and compare it with the binary fraction of the progenitor population, the main-sequence stars. If the binary fraction of CSPNe were higher than the prediction based on the progenitor population, this would imply that PNe are indeed preferentially formed via a binary channel.

The short-period, post-common-envelope binary fraction, 15–20 per cent, was determined by two-independent photometric close-binary surveys (Bond 2000; Miszalski et al. 2009a,b). This fraction is however limited to very short periods. Estimating the fraction of CSPN that are in binaries with any separation requires an efficient method for detecting binaries, a reasonable sample size and a clear understanding of the intrinsic biases of the method and sample. Our

⋆ E-mail: dimitri.douchin@mq.edu.au

ultimate goal is to find the fraction of CSPN with binary companions at any separation, which is best done using the near-infrared (NIR) excess method, even if this technique cannot detect hot, evolved companions. This technique offers the distinct advantage of being unbiased with respect to binary separation. The technique, however, requires the availability of excellent quality data obtained in perfect weather in order to detect per cent-level flux excess.

This method has been used in the past with mixed results (e.g. Zuckerman, Becklin & McLean 1991). More recently, Frew & Parker (2007) and Frew (2008) attempted to determine the binary fraction using the volume-limited sample of Frew (2008) and a compilation of magnitudes from the literature but with particularly careful vetting. They detected 17 objects with *J*-band excess out of 32 sampled CSPN, but their biases were unquantified. In the first paper in this series (De Marco et al. 2013, hereafter Paper I), we searched for *I*- and *J*-band flux excess in a sample of 27 CSPN for which data were purposefully obtained, and detected 9 *I*-band flux excess objects, sometimes at a low sigma significance. A subsample of nine objects with 2MASS, *J*-band data (more sensitive to reveal cool companions) were also analysed and this exercise confirmed low sigma *I*-band detections as well as revealed a few others, which were not detected in the *I* band.

To improve on the results of Paper I, we use new observations of ∼20 CSPNe observed in the *U*, *B*, *V* and *I* bands to extend the sample of our NIR excess study of CSPN using the 3-kpc volume-limited sample of Frew (2008). A statistically large enough sample ($\gtrsim$100) is necessary to draw conclusive observations regarding the binary fraction. An overlap between the two samples is also important to calibrate any systematics. Furthermore, we refine our magnitude measurement method by using point spread function (PSF) photometry as opposed to aperture photometry. Finally, by analysing some objects that are at the limit of our selection criteria we are able to quantify the method's uncertainties, such as issues with accurate background subtraction.

In this paper, we also attempt to use archival data from the Sloan Digital Sky Survey (SDSS) Data Release 7 (DR7; Abazajian et al. 2009), to both confirm detections and limits of our sample and to potentially extend the sample size. In the near future, the photometric data from the new VPHAS+ Survey of the southern Galactic plane (Drew et al. 2014) will allow us to apply the NIR excess method to many more CSPN, adding statistical weight to this approach.

In Section 2, we describe our observations and data reduction. We explain the details of our photometric treatment and the calibration of these fluxes in Section 3. Objects that have been excluded from our sample due to complications during the flux measurements are presented in Section 4. The refined technique for *I*- and *J*-band excess detections is presented in Section 5. Section 6 covers the use of SDSS for discovering new red flux (*z*-band) excess objects. We estimate the binary fractions of CSPN from our entire sample and refined technique in Section 7. Notes on individual objects are given in Section 8 before concluding in Section 9.

2 OBSERVATIONS AND DATA REDUCTION

Our Johnson–Cousins *U*, *B*, *V* and *I* images were taken during a seven night observing run at the National Optical Astronomical Observatory (NOAO) 2.1-m telescope at Kitt Peak between 2011 March 11 and 17. Only nights 1, 4 and 6 were partially photometric and the results we present here derive from these photometric data only. During nights 2, 3, 5 and 7 and non-photometric parts of nights 1, 4 and 6 we carried out photometric monitoring of those targets that will be presented in a later paper. We used the optical camera T2KB, with 2048 × 2048 pixels yielding a field of view of 6.5 arcmin × 10 arcmin on the sky after cropping (we used T2KB default sampling of 0.3 arcsec pixel^{-1}). The pixel size is 24 μm with a typical readout noise of 4 electrons rms. We used a gain of 1.04 electrons ADU^{-1} with a pixel saturation of 65 000 ADU.

The images have been reduced using the standard *ccdproc* procedure provided within the software IRAF[1] allowing debiasing, overscanning and flat-fielding. A total of 10 bias frames have been taken at the beginning of each night as well as 10 dome-flat images in each filter at the beginning and end of each night. The dark current noise of the T2KB CCD, $<$ 4 electrons h^{-1} pixel^{-1}, is negligible in comparison with the other sources of noise expected in our data; therefore, no dark-frame subtraction has been used in the reduction process, although dark images have been acquired for precaution in the morning after each observation. The logs of the photometric observations are provided in Appendix A.

2.1 Target selection

As in Paper I, the target list is drawn from the volume-limited sample of Frew (2008) updated by Frew (in preparation). The distances have been determined thanks to an improved Hα surface brightness–radius relation (Frew, Bojičić & Parker 2013), and yields a precision of ∼20 per cent on average. In addition, as in Paper I we have mostly observed CSPN with old, extended (more than 25 arcsec), faint PN around them, while avoiding compact, dense PN for which it is difficult to achieve accurate background subtraction. We have also chosen our targets to have an absolute *V* magnitude, $M_V \gtrsim 5$, if possible, both to avoid wind-induced variability in intrinsically bright CSPN and to enable the detection of intrinsically faint companions. Objects within ∼10 deg of the Galactic plane have been largely excluded to avoid crowded fields, limiting the possibility of a field star aligning with our targets. When a target was close to the Galactic plane, the field was inspected to insure that the crowding was a minimum. To attempt an unbiased sample, we did not inspect the names of our targets until we had a target list answering to the selection criteria. This means that occasionally a known binary is included in our list. Such inclusion provides us with a check on the detection technique.

Due to telescope size limitations, our targets have apparent *V* magnitudes between 14 and 20. These criteria of selection constitute an intrinsic bias to be remembered when extrapolating our results to the entire PN population. The list of our targets, along with their properties, is given in Table 1.

We have used a selection of equatorial Landolt photometric standards (Landolt 1992) containing blue stars when possible and standards situated in non-crowded regions to allow the best possible photometry. The list of the standards we used is presented in Table 2. We have observed one standard before and after each target to insure a satisfying coverage in airmass along our observing window. Unfortunately, we observed only few standards at high airmass (∼2) and this limited the fit accuracy. In Table 3 we list the best available *J*, *H* and *K* magnitudes for a subset of our sample from extant surveys.

[1] Image reduction and analysis facilities, http://iraf.noao.edu/

Table 1. New and updated parameters for our targets. See Section 8 and Appendix D for details on individual objects. The same stellar parameters as in Paper I have been used for the targets in common.

Name	Sp. type[a]	PN[b] morph.	D[c] (kpc)	M_V (mag)	E(B − V) (mag)	T_{eff} (method) (kK)	log g (cm s^{-2})	Reference
Abell 39	hgO(H)	R	1.4	4.8	0.02	117 ± 11 (m)	6.28 ± 0.22	Napiwotzki (1999)
EGB 9†	–	I	0.34	4.6	≤0.056[d]	–	–	Ali et al. (2012)
FP J1824-0319	DA	Ra	0.29	7.3	–	–	–	–
H 4-1•	–	E	–	–	–	82 ± 2 (tzHeII)	–	Phillips (2003)
HaWe 10	hgO(H)	R	3.01	5.5	0.02	80 ± 10 (s)	8.0:	Girven et al. (2011)
IC 972•	–	Rr	2.78	2.4	–	89 ± 11 (tzHeII)	–	Phillips (2003, 2004)
IC 3568•	O3(H)	Rs	2.71	–	0.17	50 ± 5 (m)	4 ± 0.2	Gabler, Kudritzki & Mendez (1991)
IC 4593•	O7(H)	Ra	1.57	–	0.07	49 ± 2 (tzHeII)	–	Phillips (2003)
Jacoby 1	PG1159	Ra	0.57	6.8	0.02	150 ± 10	7.0 ± 0.4	Jacoby & van de Steene (1995)
LTNF 1	O(H) + K5: V	B	2.00	3.23	0.03	105 ± 11 (s)	6.5 ± 0.25	Liebert et al. (1995)
Na 1•	–	E	–	–	–	43 ± 10 (tzHeI)	–	Phillips (2003)
NGC 6058	O9(H)	Ebp	2.73	1.6	0.03	77 (m)	4.8 ± 0.3	Herald & Bianchi (2011)
NGC 6781	hgO(H)	Eb	0.75	5.7	0.61	104[e] (tzHeI)/123 ± 9 (m)	–	Schwarz & Monteiro (2006)
Sa 4-1•	O(H)	R	–	–	–	75 ± 10 (s)	7.9[c]	Feibelman & Bruhweiler (1989)
Sh 2-68†	PG1159	I	0.7[f]	5.6	–	96 ± 9 (m)	6.78 ± 0.32	Napiwotzki (1999)
Sh 2-216•	DAO	Ra	0.129[g]	6.83[g]	0.08[g]	95 ± 2 (m)	6.9 ± 0.2	Harris et al. (2007)
SkAc 1	–	Rc	1[h]	8.5	–	–	–	–
We 2-34	–	Bap:	1.59	7.7	–	–	–	–

[a]The spectral types are from Weidmann & Gamen (2011).
[b]The morphological classes are mainly from Frew (2008), based on the scheme of Parker et al. (2006).
[c]Distances, M_V, E(B − V) and temperatures are from Frew (2008) unless otherwise indicated.
[d]Schlafly et al. (2010).
[e]Phillips (2003).
[f]Ali et al. (2012).
[g]Rauch et al. (2007).
[h]Assumed value.
•Excluded from sample for statistics, †Mimic.

Table 2. Landolt standards used for our observing run.

Name	No. of stars (incl. no. of blue stars)	Observed nights
100 280	2	6
107 601	3	1, 6
G163	2	1, 6
PG0918+029	5 (1)	1, 4
PG1034+001	1 (1)	1, 6
PG1323-085	4 (1)	1, 4, 6
PG1633+099	5 (1)	1, 4, 6

Table 3. Near IR magnitudes from the 2-micron All Sky Survey (2MASS) and the UKIRT Deep Sky Survey (UKIDSS).

Object	J (mag)	H (mag)	K (mag)	Data source
A 39	16.30 ± 0.10	16.41 ± 0.02	16.55 ± 0.05	UKIDSS
IC 972[a]	15.78 ± 0.07	15.41 ± 0.11	15.16 ± 0.14	2MASS
FP J1824-0319	15.51 ± 0.07	–	–	2MASS
Jacoby 1	16.38 ± 0.12	–	–	2MASS
LTNF 1	13.96 ± 0.03	13.71 ± 0.03	13.63 ± 0.03	2MASS
NGC 6058	14.46 ± 0.04	14.62 ± 0.06	14.58 ± 0.10	2MASS
NGC 6781	16.24 ± 0.11	<14.61	<14.96	2MASS
Sh 2-68[b]	16.04 ± 0.10	16.01 ± 0.17	–	2MASS
SkAc 1	18.50 ± 0.05	18.16 ± 0.05	18.27 ± 0.13	UKIDSS
We 2-34	18.47 ± 0.05	17.58 ± 0.04	17.53 ± 0.10	UKIDSS

[a]Excluded from sample for statistics; [b]Mimic.

3 THE DETERMINATION OF THE PHOTOMETRIC MAGNITUDES

3.1 Determination of the instrumental magnitudes

Accurate reduction and calibration is an essential element for NIR excess detections in the visible and NIR spectral bands. Several techniques are available for this purpose. We used DAOPHOT Stetson (1987), that uses PSF-fitting photometry. Below is a description of how we chose input parameters for DAOPHOT to obtain our magnitudes. Default values along with our adopted values for the various parameters described in this section are listed in Table 4. Stars used to choose these parameters are listed in Table 5.

DAOPHOT photometry is performed in five steps: FIND, PHOT, PICK, PSF and ALLSTAR. The routine FIND detects the stars in the image by convolving the image with a Gaussian curve with width provided as input by the user. This allows a clearer detection of peaks and more accurate selection of the source type (stellar or extended; Stetson 1987). Positive features in the convolved image are detected as potential centroids if the height of their central pixel has a value greater than n times the noise value, it is considered and the surrounding pixels intensity is integrated. In DAOPHOT, n is input by the user as the THRESHOLD (TH) parameter. The noise value is taken to be the mode of a distribution of 10 000 clipped, random pixels in the image. The input parameters required by FIND are RE, GA, LO, HI, FW, TH, LS, HS, LR, HR and WA. RE, GA and HI have been assigned as per the CCD characteristics, FW has been chosen to be the median PSF in the image (later FWHM), whereas all the other parameters have been setup with the default values given in Stetson (2000), allowing satisfactory source detection (see Table 4).

Table 4. DAOPHOT input parameters.

ID	Description (note)	Routines affected	Permitted values	Default value	Our adopted value
RE	Readout noise, 1 exposure (ADU)	FIND	Positive	0	4.57
GA	Gain, 1 exposure (photons per ADU)	FIND	Positive	0	1.04
LO	Low good datum (standard deviations)	FIND	Non-negative	7	5
HI	High good datum (ADU)	FIND	Non-negative	32 766.5	50 000
FW	FWHM of objects for which FIND is to be optimized (in pixels)	FIND	0.2–15.0	2.5	1 FWHM
TH	Significance threshold for detection (standard deviations)	FIND	Non-negative	4.0	5.0
LS	Low sharpness cutoff	FIND	0.0–1.0	0.2	0.2
HS	High sharpness cutoff	FIND	0.6–2.0	1.0	1.0
LR	Low roundness cutoff	FIND	−2.0–0.0	−1.0	−1.0
HR	High roundness cutoff for the profile fits	FIND	0.0–2.0	1.0	1.0
WA	Watch progress of reductions on terminal	FIND, PHOT, PEAK, PSF NSTAR, SUBSTAR, SORT	−2–2	1	−1 (non-interactive mode)
FI	The fitting radius (in pixels)	PSF, PEAK, GROUP, NSTAR	1.0–10.0	2.0	2×FWHM
PS	PSF radius: radius (in pixels) within which the PSF is to be defined	PSF	1.0–35.0	11.0	4 ×FWHM
VA	Degree of variation in the PSF	PSF	−1–2	0	0
AN	Which analytic formula for PSF	PSF	1–6	1	1
EX	How many passes to clean discordant pixels from the PSF table(s)	PSF	0–9	0	5
PE	Per cent error (e.g. flat-field)	PEAK, NSTAR	0–100	0.75	0.75
PR	Profile error (inadequate PSF)	PEAK, NSTAR	0–100	5.0	5.0
IS	Inner radius of annulus for background estimation	PHOT, PSF	0-OS	2.0	4 FWHM
OS	Outer radius of annulus for background estimation	PHOT, PSF	0-n/a	PS	5 FWHM

Table 5. PNe used for the determination of optimal DAOPHOT parameters.

PN Name	*V*	Bright nebula
A 28	16.5	No
JnEr 1	17.1	No
LTNF 1	15.2	No
NGC 6781	16.8	Yes
We 2-34	19.4	No

The routine PHOT performs aperture photometry in a traditional way on the sources detected by FIND. The user defines as input the aperture(s) (AP1(,AP2,...)) within which to sum the counts around the centroid and the inner and outer radii of the sky annulus determination, respectively, IS and OS. The sky counts are determined from the annulus and subtracted from the stellar counts integrated in the central aperture. The output of the aperture photometry step is used as input files for the PICK and PSF routines. We found the choice of the aperture to have no influence on the final magnitudes, consistent with the fact that this photometry is then refined by the PSF-fitting process.

The routine PICK is used to determine which stars will contribute in estimating the model PSF in the image. The user can choose to keep only the NSTAR brightest stars in the field, or to select a lower limit for the instrumental magnitude. For each star selected, an analytic model of the PSF is fitted to the star (parameter AN, by default AN = 1, implying a bi-variate Gaussian) and subtracted; then, the residuals from the analytic solution are interpolated every half pixel and subtracted also from the sky level. The instrumental magnitude for a given model PSF star is the sum of these two contributions. This step is somewhat similar to the aperture correction step in aperture photometry where the sources with the best signal-to-noise ratio are used to adjust the PSF wing contribution. The default instrumental magnitude is 13 and we have kept this value as it provides a sufficient number of PSF stars (typically 10; Stetson 1987 recommends a strict minimum of 3). All PSFs of the stars selected by PICK are averaged to create a model PSF for the image using the routine PSF. This model PSF for the image is then applied to all the detected stars in the image using PSF.

The routine ALLSTAR is used to determine the actual instrumental magnitude of the stars. It uses the PSF modelled with PSF and scales it to each star detected with FIND. The two main parameters are the PSF radius (PS) which quantifies the spatial extent of the star on the image and the fitting radius (FI), which defines the region that will be used when scaling the model PSF to the field star. The PSF radius can be determined by the limit radius at which the PSF wings blend with the background. Experimentation with our data led us to use a PSF radius of four times the FWHM (full width at half-maximum). The fitting radius by definition smaller than the PSF radius is the portion that is considered with certainty being 'good data' in the observed PSF. We have chosen FI = 2 × FWHM, which is the threshold at which the magnitude does not change with increasing FI, while being consistently smaller than the PSF radius. The magnitude determination works as follows: all the pixels in the PSF radius are fitted analytically as described above, while the deviation from the analytic model is interpolated only in the fitting radius region. At each iteration, all the measured PSF are subtracted from the image creating a residual image. On this residual image, the star-finding procedure is applied to detect stars that would have been blended together in the original image. The stars are being added to the list of measured stars. Iteratively, source detection, aperture photometry, PSF-modelling, PSF-fitting and subtraction are applied until all signal identified as stars has been detected. The sky background is determined every three iterations in the annulus given in input (IS and OS, Table 4), after the detected stars have been subtracted. Note that this allows one to take into account the background photons behind the star (as the star has been removed). The inner radius of the background annulus can thus be inside the fitting radius and allows the integration of more backgrounds counts than an annulus around the object, as in standard aperture photometry. However to be sure, we chose to pick our inner background outside of the PSF radius.

Table 6. Calibration coefficients for the photometric nights of observations.

Night	Filter	Zero-point (O)	Colour-index (C)	Atmospheric absorption (K)	No. of standards observed
1	U	24.212 ± 0.032	0.058 ± 0.004	0.711 ± 0.024	35
	B	25.305 ± 0.032	0.066 ± 0.007	0.270 ± 0.024	34
	V	25.401 ± 0.023	−0.015 ± 0.005	0.120 ± 0.017	46
	I	24.492 ± 0.028	−0.001 ± 0.005	0.015 ± 0.020	40
4	U	24.019 ± 0.031	0.033 ± 0.008	0.556 ± 0.023	26
	B	25.234 ± 0.027	0.056 ± 0.008	0.227 ± 0.019	37
	V	25.436 ± 0.020	−0.028 ± 0.006	0.148 ± 0.014	37
	I	24.532 ± 0.030	−0.008 ± 0.009	0.059 ± 0.022	43
6	U	24.000 ± 0.022	0.038 ± 0.006	0.497 ± 0.015	53
	B	25.331 ± 0.015	0.059 ± 0.005	0.242 ± 0.011	45
	V	25.468 ± 0.016	−0.023 ± 0.005	0.113 ± 0.011	46
	I	24.604 ± 0.021	0.006 ± 0.006	0.066 ± 0.015	40

3.2 Calibration of the instrumental magnitudes

The calibration of the instrumental magnitudes is similar to the one described in Paper I except that the filters used here are U, B, V and I and not B, V, R and I. The resulting photometric system is therefore:

$$\begin{aligned} U &= O_U + u + C_U(U-B) - K_U \times Z_U \\ B &= O_B + b + C_B(B-V) - K_B \times Z_B \\ V &= O_V + v + C_V(B-V) - K_V \times Z_V \\ I &= O_I + i + C_I(V-I) - K_I \times Z_I \end{aligned} \quad (1)$$

where O, C and K are the calibration coefficients, O_U, O_B, O_V, O_I are the instrumental offsets, C_U, C_B, C_V, C_I are the colour terms, K_U, K_B, K_V, K_I are the extinction coefficients, and Z is the airmass of the observation. These coefficients were determined for each night (Table 6) by using a standard least-squares procedure in order to solve numerically the system in equation (1) for our selection of Landolt standards (Table 2). To insure a photometric solution as accurate as possible, outliers have been visually removed through a series of sanity checks (see Fig. 1) when estimating the standard solution. The values of the calibrated magnitudes and errors for each night are provided in Appendix B. The averaged magnitudes have followed the same statistical treatment as in Paper I. The final calibrated magnitudes were calculated as the weighted average of the calibrated magnitudes on the different nights. For a given calibrated magnitude in a given bandpass, the error is defined as

$$\begin{aligned} \sigma_U^2 &= \sigma_{O_U}^2 + \sigma_u^2 + \sigma_{C_U}^2(U-B)^2 + \sigma_{U-B}^2(C_U)^2 \\ &\quad + \sigma_{K_U}^2 Z_U^2 + \sigma_{Z_U}^2 K_U^2 \\ \sigma_B^2 &= \sigma_{O_B}^2 + \sigma_b^2 + \sigma_{C_B}^2(B-V)^2 + \sigma_{B-V}^2(C_B)^2 \\ &\quad + \sigma_{K_B}^2 Z_B^2 + \sigma_{Z_B}^2 K_B^2 \\ \sigma_V^2 &= \sigma_{O_V}^2 + \sigma_v^2 + \sigma_{C_V}^2(B-V)^2 + \sigma_{B-V}^2(C_V)^2 \\ &\quad + \sigma_{K_V}^2 Z_V^2 + \sigma_{Z_V}^2 K_V^2 \\ \sigma_I^2 &= \sigma_{O_I}^2 + \sigma_i^2 + \sigma_{C_I}^2(V-I)^2 + \sigma_{V-I}^2(C_I)^2 \\ &\quad + \sigma_{K_I}^2 Z_I^2 + \sigma_{Z_I}^2 K_I^2. \end{aligned} \quad (2)$$

The weights for averaging magnitudes at different epochs are defined as the inverse of the uncertainty for a given measurement σ_b normalized by the sum of the weights. The error on the averaged calibrated magnitudes is the weighted standard deviation of the averaged calibrated magnitudes on the different nights (see Paper I). When the target has been observed only once (this is the case for about half of our CSPNe), we used the quadratic sum of the instrumental photometric error and the errors from the calibration as a value for the error on the magnitude. For our faintest objects no U-band images have been taken due to the longer exposure times required in this band.

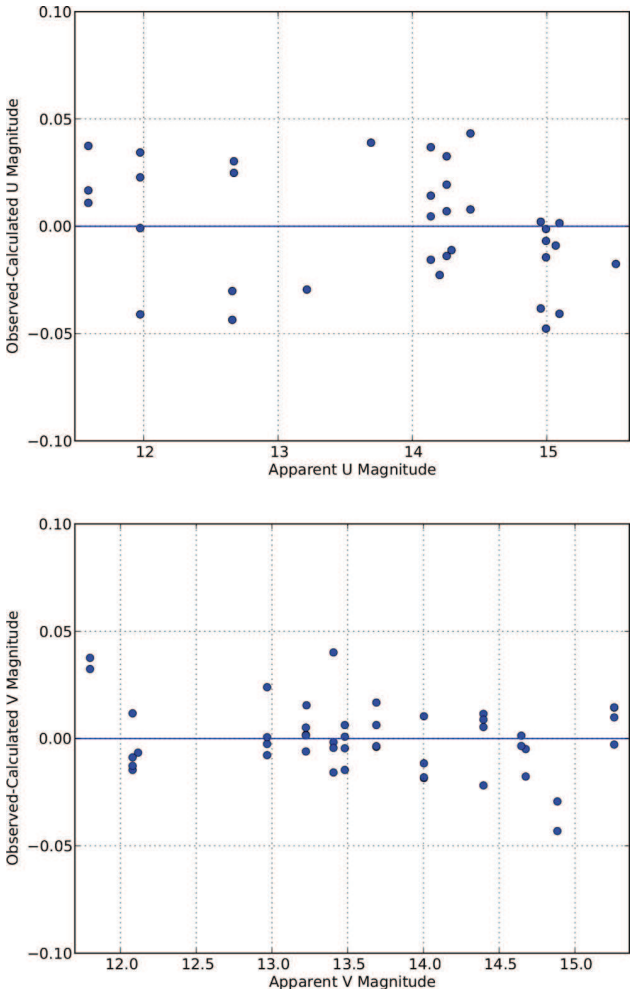

Figure 1. Comparison of our calibrated magnitudes with the ones obtained by Landolt (1992). The upper panel shows the dispersion in the U band for Night 1 – expected to be less good than the lower panel – the dispersion in the V band for Night 6.

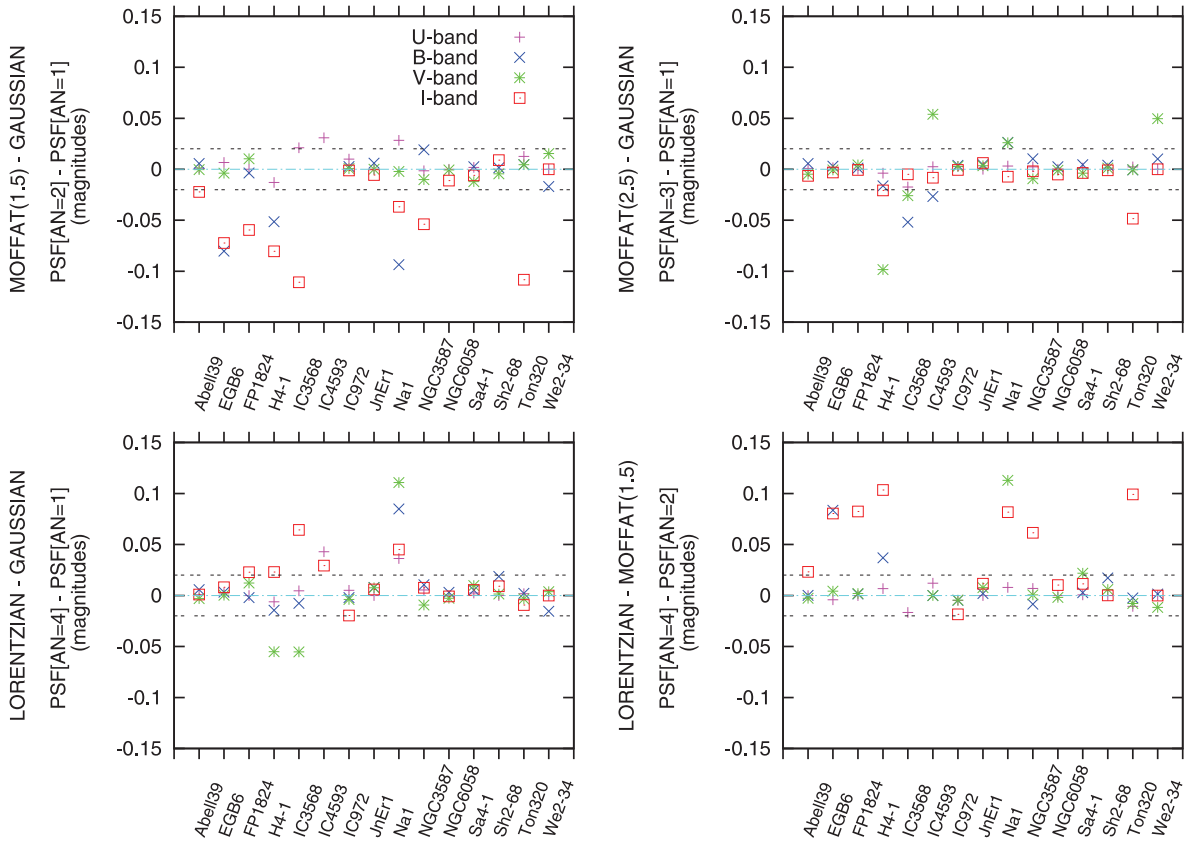

Figure 2. Change of the calibrated magnitudes of the Night 6 objects using different values for the parameter AN (Table 4; AN = 1, Gaussian; AN = 2, Moffat function with a 1.5 index; AN = 3, Moffat function with a 2.5 index; AN = 4, Lorentzian function.) The difference between the magnitudes obtained with values of AN = 1 and 3 show the least scatter, whereas the difference between the magnitudes obtained with AN = 2 and other values of AN display a larger scatter. A value of AN = 1 has been adopted for our photometry, although a value of 3 would have also been acceptable. It is also apparent that H 4-1, IC 3568, IC 4593 and Na 1 show a greater sensitivity to input parameters due to their bright and/or compact PN (see Section 4 and Appendix D).

Our targets showed a typical scatter of • 0.02 calibrated magnitudes when varying DAOPHOT input parameters (e.g. PS, FI, AN and IS, see Fig. 2 for the variations of calibrated magnitudes with respect to the PSF analytic function parameter AN). These variations of the magnitudes with respect to input photometric parameters are partly accounted for in the errors given in Table 7 because they would have affected the standards' calibration. We also guard against poorly quantified errors by relying on multiple observations and observations on multiple platforms (see Section 6).

To check the consistency of our photometry, we report in Table 8 (see also Fig. 3) the magnitudes of objects that have been observed both during this observing run and the one of Paper I: A 28, EGB 6, JnEr 1, NGC 3587, Ton 320 and WeDe 1 (Table 5). In the *B* and *V* bands, the agreement is better than • 0.03 mag and is mostly justified by the error bars. In the *I* band, the disagreement is as large as 0.06 mag, with half the objects within the 0.03-mag limit. The error bars cannot explain all of these discrepancies. The reason for these discrepancies can be varied, including intrinsic low-level variability. For the time being, we average all values and adjust the error accordingly (see Section 3.2). We discuss further our sources of uncertainty in Section 5.1.

Additionally, two of our objects, JnEr 1 and NGC 6058, have been observed by the *Hubble Space Telescope* and their *V* and *I* magnitudes have been reported by Ciardullo et al. (1999). Our magnitudes are consistently brighter by 0.05 mag for both objects. Their *V* • *I* colours are in agreement with ours within 0.02 mag, a reasonable agreement given the difference in filters and method used to obtain these colours.

4 REJECTED TARGETS

Our goal is to provide a more robust estimate of the CSPN binary fraction using the NIR excess method by extending the analysis of Paper I to a bigger sample. In an effort to add objects to our sample, we observed targets that were at the limit of our selection criteria. As a result, our sample included a few distant, compact PN (H 4-1, Na 1, Sa 4-1) and some CSPNe surrounded by bright nebulae (IC 3568, IC 4593 and IC 972). These features represent a challenge to our analysis primarily because of the difficulty of subtracting the nebula. We have analysed these objects to quantify the problem, but they are rejected from the final analysis.

Objects with a bright and compact PN suffer from nebular contamination as the PN cannot be adequately subtracted. Objects with a bright *extended* PN result in either too much nebular subtraction, when the nebular light overlapping the stellar PSF is less than the light sampled in the background region, or, more commonly, too little nebular subtraction if the opposite takes place. Nebular contamination affects the *B* band (Hβ is included in the bandpass as well as the [O III] λ5007 at the red end of the bandpass) and its *V* band (which includes the λ5007 [O III] line in the middle of the wavelength range). In most cases, the *V* band will be more affected than the *B* band. The *U* and *I* bands are less affected by PN line

Table 7. Calibrated magnitudes for our sample. The targets common with Paper I are listed first. For these objects, the photometric measurements of Paper I have been averaged with the new ones (see Appendix B). The numbers in parenthesis indicate the number of epochs of observation. The PN names in parenthesis are mimics or objects that have been observed but excluded from our final sample. See Section 4 and Appendix D for an explanations of individual objects.

Object	U	B	V	I
A 28	15.153 ± 0.009(1)	16.277 ± 0.007(4)	16.543 ± 0.017(4)	16.855 ± 0.022(4)
EGB 6	14.465 ± 0.010(2)	15.690 ± 0.001(4)	15.997 ± 0.005(4)	16.319 ± 0.014(4)
JnEr 1	15.519 ± 0.008(1)	16.759 ± 0.013(4)	17.116 ± 0.014(4)	17.491 ± 0.015(4)
NGC 3587	14.148 ± 0.008(2)	15.400 ± 0.011(5)	15.774 ± 0.008(5)	16.172 ± 0.022(5)
Ton320	14.156 ± 0.009(2)	15.366 ± 0.011(4)	15.704 ± 0.016(4)	16.063 ± 0.031(4)
WeDe 1	–	16.961 ± 0.018(2)	17.225 ± 0.004(2)	17.463 ± 0.031(3)
Abell 39	14.129 ± 0.005(2)	15.314 ± 0.003(2)	15.616 ± 0.002(2)	15.929 ± 0.004(2)
(EGB 9)[a]	12.863 ± 0.009(1)	13.062 ± 0.008(1)	13.133 ± 0.009(1)	13.037 ± 0.010(1)
FP J1824-0319	–	14.601 ± 0.006(1)	14.841 ± 0.004(1)	15.159 ± 0.010(1)
(H 4-1)[b]	15.971 ± 0.019(1)	16.704 ± 0.183(2)	15.571 ± 0.155(2)	17.580 ± 0.117(2)
HaWe 10	–	17.549 ± 0.008(1)	17.888 ± 0.005(1)	18.259 ± 0.009(1)
(IC 3568)[c]	11.3 ± 0.1(1)	12.2 ± 0.1(1)	12.2 ± 0.1(1)	12.7 ± 0.1(1)
(IC 4593)[c]	9.7 ± 0.1(1)	–	–	11.1 ± 0.1(1)
(IC 972)[c]	17.8 ± 0.1(1)	18.0 ± 0.1(1)	17.4 ± 0.1(1)	16.5 ± 0.1(1)
Jacoby 1	13.963 ± 0.005(1)	15.216 ± 0.008(1)	15.610 ± 0.005(1)	16.020 ± 0.010(1)
LTNF 1	14.610 ± 0.011(1)	15.739 ± 0.007(1)	15.746 ± 0.006(1)	15.269 ± 0.008(1)
(Na 1)[b]	15.810 ± 0.036	16.310 ± 0.084	15.570 ± 0.102	15.879 ± 0.0.060(1)
NGC 6058	–	13.452 ± 0.004(1)	13.802 ± 0.004(1)	14.169 ± 0.007(1)
NGC 6781	16.243 ± 0.039(1)	17.111 ± 0.021(1)	16.880 ± 0.016(1)	16.439 ± 0.029(1)
(Sa 4-1)[b]	12.249 ± 0.004(1)	13.427 ± 0.004(1)	13.721 ± 0.005(1)	14.064 ± 0.006(1)
(Sh 2-216)	11.228 ± 0.007(1)	–	–	–
(Sh 2-68)[a]	15.809 ± 0.007(1)	16.647 ± 0.010(2)	16.453 ± 0.001(2)	16.173 ± 0.020(2)
SkAc 1	–	18.192 ± 0.006(3)	18.487 ± 0.010(3)	18.563 ± 0.027(2)
We 2-34	–	19.877 ± 0.002(2)	19.836 ± 0.004(2)	19.217 ± 0.015(1)

[a]These objects were discovered to be mimics, i.e. not bona fide CSPN.
[b]These objects have compact bright PN which are not subtracted: the B and V band are the sum of the stellar and nebula fluxes.
[c]These objects have large bright PN which tend to be poorly subtracted. The errors were set to be 0.1 mag.

Table 8. Comparison of the magnitudes of objects in commom between the analysis of Paper I and this analysis. For our analysis, the magnitudes of Paper I and this analysis have been combined.

Name	B	V	I
	Paper I		
A 28	16.280 ± 0.008(3)	16.557 ± 0.009(3)	16.877 ± 0.014(3)
EGB 6	15.692 ± 0.002(2)	15.999 ± 0.002(2)	16.300 ± 0.009(2)
JnEr 1	16.775 ± 0.005(2)	17.13 ± 0.013(2)	17.501 ± 0.023(2)
NGC 3587	15.414 ± 0.001(3)	15.777 ± 0.009(3)	16.194 ± 0.029(3)
Ton 320	15.379 ± 0.007(2)	15.725 ± 0.006(2)	16.105 ± 0.018(2)
WeDe 1	16.958 ± 0.007(3)	17.226 ± 0.004(3)	17.489 ± 0.016(3)
	This paper		
A 28	16.273 ± 0.009(1)	16.523 ± 0.007(1)	16.83 ± 0.010(1)
EGB 6	15.689 ± 0.001(2)	15.997 ± 0.006(2)	16.328 ± 0.003(2)
JnEr 1	16.750 ± 0.008(2)	17.107 ± 0.008(2)	17.487 ± 0.004(2)
NGC 3587	15.390 ± 0.002(2)	15.772 ± 0.007(2)	16.161 ± 0.002(2)
Ton 320	15.360 ± 0.007(2)	15.693 ± 0.004(2)	16.05 ± 0.018(2)
WeDe 1	–	–	17.43 ± 0.022(1)

contamination. For some of the objects, the PN is still visible in the U-band images, possibly due to PN continuum emission. In the case of a very compact PN, nebular light remains in the photometry of the star and the CSPN appears too red in its B − V colour. The derived reddening will hence be too large. De-reddened V − I colours will then tend to be too blue for the stellar temperature and this will result in a 'red deficit', i.e. in a V − I colour bluer than the single star prediction. For bright extended PN, the opposite could also happen, if the nebula is oversubtracted, but this is not as common. We obtained a 'red deficit' for five of our bright compact or extended PN (H 4-1, Na 1, Sa 4-1, IC 3568 and IC 4593).

IC 972 displayed a flux excess. Despite this we abided by our selection criteria and excluded IC 972 from the sample, because the impact of nebular contamination could not be estimated. However,

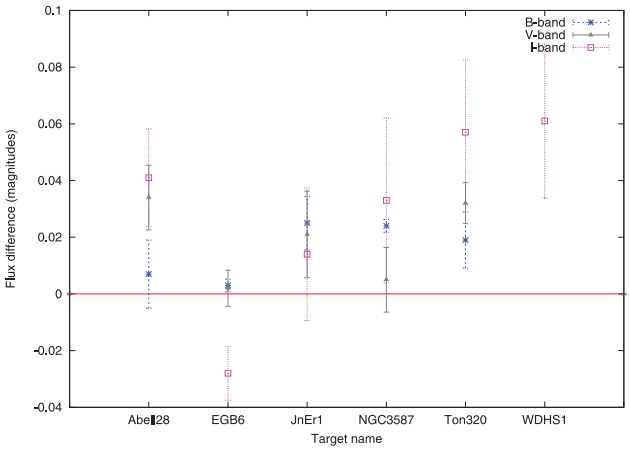

Figure 3. Magnitude difference for targets in common with Paper I. The *y*-axis shows the magnitude difference 'Paper I–Paper II'. WDHS1 = WeDe 1.

it is worth noting that this is a rather prominent flux excess, and that the binary nature of IC 972 should be reassessed.

For objects with a bright extended PN (IC 3568, IC 4593 and IC 972), we artificially increased the error to 0.1 mag in Table 7 to reflect this difficulty. We did not increase the errors on photometry of central stars of bright compact PN (H 4-1, Na 1 and Sa 4-1), because the photometry is accurate although it includes the star and nebula, something that increases the flux primarily the *B* and *V* bands. We have however marked them as unsuitable for the detection of companions as the colours are arbitrarily altered.

5 THE REFINED BINARY DETECTION TECHNIQUE BY RED AND NIR EXCESS FLUX

Our reduction and NIR excess detection technique is explained in Paper I. In summary, using vetted literature parameters for our CSPNe (Table 1, for details see Section 8 on individual objects) and our newly measured magnitudes (Tables 3 and 7), we look for flux excess in the *I* and *J* bands for our targets by comparing our de-reddened colour indices with those predicted by stellar atmosphere models for our targets. We compared the grid of theoretical colour indices as a function of stellar temperature derived in Paper I with the measured colour-indices of our targets. We used a single gravity value $\log g = 7$ for all our stars yielding a difference • 0.01 mag in the colours of those few objects with lower or higher value of $\log g$. The comparison between theoretical and observed *B* • *V* colours together with the reddening law of Cardelli, Clayton & Mathis (1989) and $R_V = 3.1$ yields the reddening of our targets, while the difference between the observed, de-reddened *V* • *I* (or *V* • *J*) and the single star model prediction yields the *I*-band (or *J*-band) excess.

In Table 1, we summarize the best available literature parameters, as well as the new values determined here. We used trigonometric distances if available (e.g. Harris et al. 2007; Benedict et al. 2009), otherwise distances were taken from Frew (2008). From the distances and de-reddened *V* magnitudes, we derived the absolute magnitude, M_V. Following Paper I, we adopted the effective temperature for each star from model atmosphere fits, averaging the results if there was more than one-independent analysis. If a model was not available, we calculated a Zanstra temperature in an identical fashion to Paper I. To do this, we used the new *V*

Table 9. Comparison of the reddening obtained using the *U* • *B* and *B* • *V* colours. See Fig. 4.

Name	$E(B \bullet V)_{UB}$	$E(B \bullet V)_{BV}$
A 28	0.13 ± 0.02	0.05 ± 0.02
A 39	0.07 ± 0.01	0.04 ± 0.01
EGB 6	0.02 ± 0.01	0.03 ± 0.01
EGB 9	1.40 ± 0.02	0.26 ± 0.01
IC 3568	0.40 ± 0.08	0.23 ± 0.09
IC 972	1.23 ± 0.04	0.94 ± 0.03
JnEr 1	0.00 ± 0.02	0.00 ± 0.02
LTNF 1	0.14 ± 0.02	0.33 ± 0.01
NGC 3587	0.00 ± 0.03	0.00 ± 0.01
NGC 6781	0.49 ± 0.06	0.56 ± 0.03
Sh 2-68	0.53 ± 0.02	0.52 ± 0.01
Ton 320	0.01 ± 0.02	0.00 ± 0.02

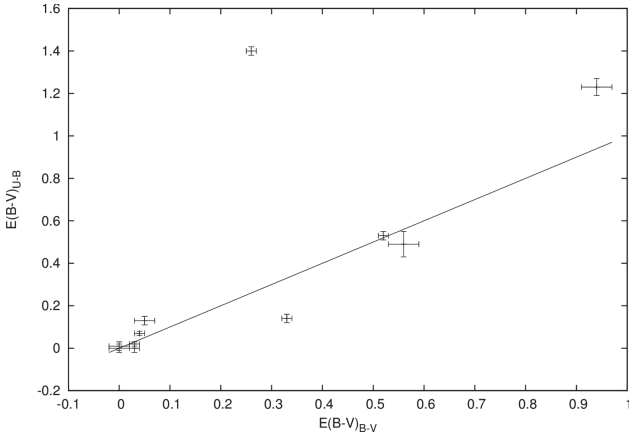

Figure 4. Comparison of the reddening obtained using the *U* • *B* and *B* • *V* colours. The values for each object are given in Table 9.

photometry reported here in combination with the integrated nebular Hα and/or the He II λ4686 fluxes. The integrated Hα fluxes were taken from Frew (2008) or Frew et al. (2013), and the He II fluxes were determined from the λ4686/λ6563 ratios measured from spectroscopy, if available. Since the Zanstra method only provides a lower limit to the stellar temperature for optically thin nebulae, we have used additional information, where appropriate, to determine the most suitable value for the temperature. We note however that for CSPN with $T_{\rm eff} \gtrsim 70\,000$ K the colours are not very sensitive to temperature.

The reddening values reported in Table 1 are derived from literature data other than the stellar *B* • *V* colour index, i.e. calculated from the nebular Balmer decrement or from the interstellar hydrogen column density.

Since we have *U*-band information for many of our targets, we have a way to check the *B* • *V*-derived reddening, using the *U* • *B* colours (Table 9). This provides a consistency check and can be beneficial in those cases when a bright companion (brighter than K0–5V; see Paper I) is present and contaminates the *V* band. Fig. 4 shows the comparison between reddening values obtained with the two colours. Only in one case, LTNF 1 (BE UMa), is the *B* • *V*-derived reddening larger. This star is a known close-binary. Although its M3V companion is not likely to contaminate the *V* band, the companion shows a hotspot (Shimanskii et al. 2008) likely contaminating the *V* band (see also Ferguson et al. 1987 and

Table 10. I-band excess for our targets ($\Delta(V-I)$), companion absolute I-band magnitudes (M_{I2}) and spectral types (or limits) of our targets.

Name	E(B − V)	$(V-I)_0$	$\Delta(V-I)$	M_{I2}	Comp. spec. type
A 28[a]	0.05 ± 0.02	− 0.37 ± 0.08	− 0.03 ± 0.08	>9.62	Later than M4
A 39	0.04 ± 0.01	− 0.36 ± 0.01	− 0.01 ± 0.01	>10.27	Later than M4
EGB 6[a]	0.03 ± 0.01	− 0.36 ± 0.03	− 0.01 ± 0.03	>11.69	Later than M5
EGB 9[b]	0.26 ± 0.01	− 0.22 ± 0.05	0.13 ± 0.05	4.14 [4.67–3.75]	G4 [G8–G0]
FP J1824-0319	0.09 ± 0.01	− 0.43 ± 0.03	− 0.08 ± 0.03	–	–
HaWe 10	0.00 ± 0.03	− 0.37 ± 0.11	− 0.04 ± 0.11	>8.59	Later than M3
Jacoby 1	0.00 ± 0.06	− 0.41 ± 0.23	− 0.06 ± 0.23	>8.92	Later than M3
JnEr 1[a]	0.00 ± 0.02	− 0.38 ± 0.09	− 0.02 ± 0.09	>10.11	Later than M4
LTNF 1	0.33 ± 0.01	0.09 ± 0.05	0.43 ± 0.05	4.35 [4.54–4.17]	G5 [G7–G4]
NGC 3587[a]	0.00 ± 0.05	− 0.40 ± 0.19	− 0.05 ± 0.19	>8.71	Later than M3
NGC 6058	0.00 ± 0.04	− 0.37 ± 0.16	− 0.04 ± 0.16	>4.10	Later than G4
NGC 6781	0.56 ± 0.03	− 0.23 ± 0.10	0.11 ± 0.10	8.50 [11.57–7.64]	M3 [M5–M1]
Sh 2-68[b]	0.52 ± 0.01	− 0.34 ± 0.06	0.00 ± 0.06	>9.04	Later than M3
SkAc 1	0.00 ± 0.06	− 0.08 ± 0.20	0.24 ± 0.21	10.33 [12.92–9.32]	M4 [M6–M4]
Ton 320[a]	0.00 ± 0.03	− 0.36 ± 0.12	− 0.03 ± 0.12	>9.85	Later than M4
WeDe 1[a]	0.06 ± 0.01	− 0.32 ± 0.04	0.04 ± 0.04	>10.71	Later than M5
We 2-34	0.37 ± 0.01	0.17 ± 0.02	0.52 ± 0.02	8.55 [8.62–8.48]	M3 [M3–M3]

[a]Updated from Paper I.
[b]Mimic.

Ferguson & James 1994 for band contamination due to the presence of hot spots). For the other three objects (A 28, IC 972 and EGB 9), the B − V-derived reddening is lower, contrary to the contamination hypothesis. In two cases, it is significantly lower (IC 972 and EGB 9). IC 972 is surrounded by a bright nebula and is one of our rejected objects due to possible nebular contamination, possibly affecting the colour determination quite dramatically. EGB 9 is a mimic (Section 8). Interestingly, the upper limit to its reddening of 0.056 mag imposed by Schlafly et al. (2010) is lower than both values obtained from the star, likely indicating internal reddening. We leave this reddening discrepancy unresolved and use the B − V-derived value as we did in Paper I. We note that while for EGB 9 we detected a bright companion, for A 28 we did not. Using higher reddening values for these objects would have decreased the excess detected for EGB 9, but not eliminated it.

5.1 I- and J-band detections

The target list for our current observations originally comprised 26 objects. However, due to the weather conditions, some overlap with the sample in Paper I, new discoveries of mimics in the observed sample (Frew & Parker 2010), technical issues and the fact that some of our targets were at the detection limit, we only add 9 new CSPN to the Paper I sample of 25 objects in the I-band and 7 to the sample of 9 from Paper I in the J band.[2]

We slightly revise the detection criterion of Paper I to be $\Delta(V-I) > \sigma_{V-I}$ rather than $\Delta(V-I) - \sigma_{V-I}$. None the less, for these objects with only one observation in each band, the error on the magnitude might be slightly underestimated (see Section 3.2) and we underline the potential risk of false detection in the case of a low-sigma detected NIR excess for these objects.

In the I band, we report four detections of flux excess in our sample of CSPN (see Table 10 and Fig. 5): a 26σ detection for We 2-34, an 8σ detection for LTNF 1 (BE UMa, already known to

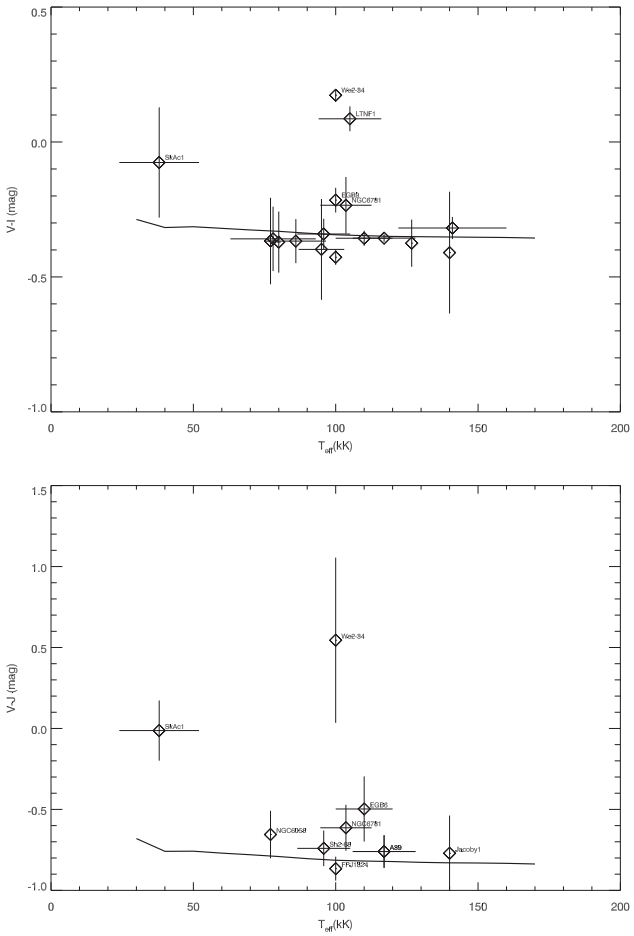

Figure 5. Top panel: predicted (solid line) versus observed (symbols) V − I colours as a function of stellar temperatures for our sample. Bottom panel: predicted versus observed V − J colours as a function of stellar temperatures for our sample.

[2] Note that the number of bona fide PN listed in Paper I (27 in the I band and 11 in the J band) has been revised here because of the discovery that two additional objects are mimics. These are EGB 1 and K 2-2.

Table 11. *J*-band excess for our targets ($\Delta(V - J)$), companion absolute *J*-band magnitudes (M_{J2}) and companion spectral types (or limits) of our targets. All detections and limits are consistent with the results of the *I*-band excess (Table 10) and of Paper I.

Name	$E(B - V)$	$(V - J)_0$	$\Delta(V - J)$	M_{J2}	Comp. spec. type
A 39	0.04 ± 0.00	− 0.76 ± 0.10	0.06 ± 0.10	>7.56	Later than M3
EGB6[a]	0.03 ± 0.01	− 0.50 ± 0.20	0.32 ± 0.20	9.03 [10.22–8.37]	M5 [M6–M4]
FP J1824-0319	0.09 ± 0.01	− 0.87 ± 0.07	− 0.05 ± 0.07	>12.26	Later than M4
Jacoby 1	0.00 ± 0.06	− 0.77 ± 0.23	0.06 ± 0.23	>8.74	Later than M5
NGC 6058	0.00 ± 0.04	− 0.66 ± 0.15	0.13 ± 0.15	>3.60	Later than G4
NGC 6781	0.56 ± 0.03	− 0.61 ± 0.14	0.20 ± 0.14	8.29 [9.77–7.55]	M4 [M6–M3]
Sh 2-68[b]	0.52 ± 0.01	− 0.74 ± 0.11	0.07 ± 0.11	>8.23	Later than M4
SkAc 1	0.00 ± 0.06	− 0.01 ± 0.19	0.73 ± 0.22	9.28 [9.97–8.59]	M5 [M6–M4]
We 2-34	0.37 ± 0.00	0.54 ± 0.51	1.36 ± 0.51	7.50 [8.32–6.82]	M3 [M4–M2]

[a]Updated from Paper I.
[b]Mimic.

be a close binary) and 1σ detections for SkAc 1 and NGC 6781. We also report a 2σ *I*-band excess for the mimic EGB 9. In the *J* band, we confirm three of the detected *I*-band detections (there is no *J*-band data for LTNF 1) with a 3.5σ detection for SkAc 1, a 2.7σ detection for We 2-34 and a 1.4σ detection for NGC 6781 (Table 11, Fig. 5). Also, the *J*-band excess for EGB 6 – already detected in Paper I – has been refined by including the newly measured magnitudes and the NIR photometry of Fulbright & Liebert (1993, see table 2 in Paper I), because their $H - K$ colour are more consistent with those of a star than those in the 2MASS data base. As a result of the larger uncertainty on their *J* magnitude, the uncertainty on the detection is larger. None the less, we obtain a similar *J*-band detection to what obtained in Paper I. The spectral types of the companions for the detections in the *I* and *J* band agree within one spectral subtype. This excellent agreement adds confidence in our analysis.

6 USING THE SDSS TO DETECT COMPANIONS TO CSPN

Ideally, we would use archival survey data, which often includes reasonable PN sample sizes, to determine the CSPN binary fraction. Unfortunately, either the precision of a given survey is not sufficient (e.g. the 2MASS survey has a limiting *J*-band magnitude of 16.5 and the error bars for magnitudes approaching this limit are large), or PN contamination of the CSPN light render the final magnitudes unreliable. Finally, the need of blue and red photometry means that many surveys can contribute to our search but are not sufficient. For example 2MASS can provide some NIR measurements, but these cannot be used to determine the potential existence of a flux excess using our method without high-quality *B* and *V* observations. Here, we carried out our analysis using SDSS data to determine the ability of this survey to detect companions. This survey is in principle ideal because it includes bands that go from the blue to the red part of the spectrum. We first analyse objects in common between our sample and the SDSS and then extend the analysis to any SDSS-observed PN.

6.1 Estimating the SDSS ability to detect faint companions

We used the photometric measurements from the SDSS DR 7 (Abazajian et al. 2009), after applying the calibration corrections described by Covey et al. (2007). These corrections are applied to the SDSS 'model' magnitudes, rather than to the PSF or Petrosian magnitudes of our objects. The corrected SDSS magnitudes are listed in Table 12.

The coefficients for the reddening (Table 13) have been obtained by convolving the SDSS filter passbands with a 100 000 K, $\log g = 7$ star, using the Cardelli et al. (1989) reddening law with $R_V = 3.1$. We

Table 12. Corrected SDSS magnitudes for targets in common with our sample (including Paper I). We used the 'model' DR7 magnitudes and applied the calibration corrections detailed in Covey et al. (2007).

Name	*u*	*g*	*r*	*i*	*z*
A 28	15.871 ± 0.004	16.291 ± 0.004	16.739 ± 0.005	17.115 ± 0.006	17.438 ± 0.017
A 31	14.674 ± 0.004	15.203 ± 0.005	15.757 ± 0.004	16.116 ± 0.005	16.396 ± 0.008
A 39	14.845 ± 0.007	15.317 ± 0.007	15.824 ± 0.007	16.201 ± 0.009	16.532 ± 0.013
EGB 6	15.199 ± 0.004	15.660 ± 0.005	16.216 ± 0.004	16.563 ± 0.004	16.906 ± 0.010
HDW 3	16.770 ± 0.004	17.019 ± 0.005	17.263 ± 0.007	17.572 ± 0.007	17.767 ± 0.017
HaWe 10	17.035 ± 0.005	17.554 ± 0.007	18.123 ± 0.009	18.532 ± 0.010	18.944 ± 0.042
IC 4593	11.804 ± 0.008	11.535 ± 0.003	11.446 ± 0.009	11.425 ± 0.004	11.969 ± 0.004
IsWe 1	16.027 ± 0.003	16.313 ± 0.004	16.640 ± 0.005	16.922 ± 0.005	17.198 ± 0.014
Jacoby 1	14.692 ± 0.003	15.237 ± 0.003	15.850 ± 0.004	16.283 ± 0.004	16.685 ± 0.009
JnEr 1	16.263 ± 0.004	16.781 ± 0.005	17.357 ± 0.006	17.756 ± 0.007	18.144 ± 0.026
K 2-2	13.524 ± 0.004	14.395 ± 0.004	14.462 ± 0.003	14.811 ± 0.005	15.153 ± 0.005
NGC 3587	14.934 ± 0.004	15.480 ± 0.004	16.046 ± 0.004	16.456 ± 0.005	16.831 ± 0.010
NGC 6058	14.029 ± 0.004	13.359 ± 0.011	14.302 ± 0.012	14.627 ± 0.005	14.771 ± 0.008
SkAc 1	17.665 ± 0.006	18.180 ± 0.009	18.651 ± 0.010	18.882 ± 0.013	19.022 ± 0.042
Ton 320	14.869 ± 0.004	15.361 ± 0.004	15.946 ± 0.004	16.328 ± 0.005	16.723 ± 0.009

Table 13. Bandpass central wavelengths after convolution with a 100 kK, log g = 7, solar abundance synthetic stellar atmosphere and resulting extinctions according to Cardelli et al. (1989).

Band	λ_0	$A_\lambda/E(B-V)$
U	3597 Å	4.86
B	4386 Å	4.12
V	5491 Å	3.10
R	6500 Å	2.10
I	7884 Å	1.90
J	1.237 μm	0.889
H	1.645 μm	0.562
K	2.212 μm	0.349
J_{2MASS}	1.241 μm	0.885
H_{2MASS}	1.651 μm	0.349
K_{2MASS}	2.165 μm	0.361
u	3586 Å	4.86
g	4716 Å	3.62
r	6165 Å	2.66
i	7475 Å	2.01
z	8922 Å	1.40

used the g − r colour to determine E(B − V) for our targets. Although the r band is more prone to contamination by a companion, the u − g colour resulted in a reddening that was systematically slightly high, producing de-reddened colours that were systematically bluer than the model colours. The u filter is known to have a red leak however this would have had the opposite effect. On the other hand, the g filter can be affected by nebular [O III] λ5007 light, which would result in too high a reddening. The model colours have been obtained using the SYNPHOT package in IRAF by convolving CSPN model spectra from TheoSSA and TMAP with temperatures between 40 and 170 kK (see Paper I) with the SDSS filters. The SDSS colours of main-sequence stars were adopted from the synthetic photometry of Covey et al. (2007). However, we did not use their approximate values for M_J, but those determined in Paper I.

Out of 15 objects in common between our sample (Paper I and this work) and the SDSS sample, we recover our detections with great consistency (A 31, EGB 6, SkAc 1, see Table 14, Fig. 6). The CSPN of SkAc 1 shows a 4σ z-band excess consistent with an M5V companion, in good agreement with the M4V companion detected at the 1σ level in the I band and the M5V companion detected at the 3σ level in the J band. EGB 6 shows a 2σ detection in the z band of an M5V companion, comparable to the 2σ M5V companion detected in the J band. A 31 shows a 4σ detection of an M4V companion, comparable to the 5σ M4V companion detection in the J band (Paper I).

It is possible that the reddening obtained from the g − r colour is slightly too high since both bands are affected by nebular lines, but the g band more so (the bright [O III] λ5007 line tends to be brighter than Hα), implying too high a reddening and yielding a 'red deficit' on stars with no NIR excess or diminishing the excess if there is one. This may be reflected by the existence of small 'red deficits' for A 28, HaWe 10 and IsWe 1 (see Fig. 6), or in some cases by SDSS companion limits being one spectral type cooler than those derived in the I- and J-band study (e.g. Jacoby 1 or JnEr 1). HDW 3 (HaWe 4) shows a puzzling 'red deficit' that cannot be accounted for by this effect nor by nebular contamination. It is uncertain why the SDSS photometry is inconsistent with that using the B, V and I bands in Paper I.

The difference in spectral type lies in the difficulty of calibrating the SDSS colours. This caveat eventually hampers detection of faint companions but guards us from a false detection. The SDSS g and r images of IC 4593 and K 2-2 show strong nebular emission explaining the strong 'red deficit' for these objects. The reddening obtained for NGC 6058 is E(B − V) = − 0.4, and clearly wrong. and the object has been excluded from the study. We conclude that provided that no nebular contamination affects the central star photometry, the SDSS photometry can be used safely to detect NIR excess with the precision of one companion spectral type.

6.2 New infrared excess detections using SDSS

With knowledge of the limitations likely to affect the SDSS we have established in Section 6.1, we used the SDSS survey to search for CSPN with z-band excess. We cross-matched the sample of Frew (2008) with the SDSS DR7 photometric catalogue. In this pilot study, we used distances from Frew (2008) or assumed a distance of 1 kpc for the one object where a value is not available, we used temperatures from Frew (2008) or Phillips (2003) and assumed a temperature of (100 000 ± 10 000) K and log g = 7 for stars with no alternative value. The magnitudes are presented in Table 15 and the results in Table 16 and Fig. 7.

A majority of the objects displaies a 'red deficit', due to too high a reddening. Small 'red deficits' can be due to the SDSS-calibration errors discussed above. It is the case for the central stars of A 13, A 33, K 1-16, KLW 10, Kn 61, KUV 03459+0037, NGC 6894 and WPS 54 (also known as PG0931+69). We have left these objects in the result table (Table 16).

Table 14. g − z excess for objects in our sample (including Paper I).

Name	E(B − V)	$(g-z)_0$	$\Delta(g-z)$	M_{z2}	Comp. spec. type
A 28	0.12 ± 0.01	− 1.41 ± 0.03	− 0.08 ± 0.04	–	–
A 31	0.01 ± 0.01	− 1.22 ± 0.03	0.12 ± 0.03	9.88 [10.23–9.58]	M4 [M4–M4]
A 39	0.07 ± 0.01	− 1.38 ± 0.04	− 0.02 ± 0.04	>10.13	Later than M4
EGB 6	0.02 ± 0.01	− 1.29 ± 0.03	0.06 ± 0.03	11.13 [11.76–10.70]	M5 [M5–M5]
HDW 3	0.33 ± 0.01	− 1.47 ± 0.03	− 0.17 ± 0.03	–	–
HaWe 10	0.00 ± 0.01	− 1.39 ± 0.06	− 0.09 ± 0.06	–	–
IsWe 1	0.25 ± 0.01	− 1.45 ± 0.04	− 0.10 ± 0.06	–	–
Jacoby 1	0.00 ± 0.04	− 1.45 ± 0.14	− 0.09 ± 0.14	>10.90	Later than M5
JnEr 1	0.00 ± 0.01	− 1.37 ± 0.04	− 0.01 ± 0.04	>11.72	Later than M5
NGC 3587	0.00 ± 0.01	− 1.36 ± 0.03	− 0.01 ± 0.03	>11.82	Later than M5
SkAc 1	0.07 ± 0.01	− 0.99 ± 0.06	0.25 ± 0.06	10.64 [11.06–10.31]	M5 [M5–M4]
Ton 320	0.00 ± 0.03	− 1.36 ± 0.11	− 0.06 ± 0.11	>11.05	Later than M5

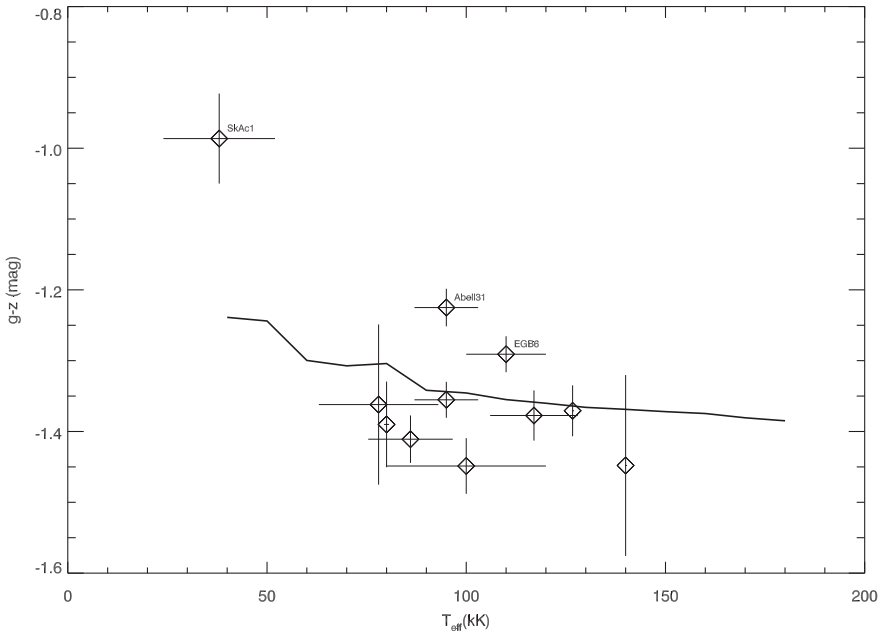

Figure 6. Predicted (solid line) versus observed (symbols) g • *z* colours as a function of stellar temperatures for those of our l-band sample targets in common with the DR7 SDSS CSPN. All symbols whose position below the line is not justified by the error bar are 'red deficit' objects caused by nebular contamination (see text).

Table 15. Corrected SDSS magnitudes for targets in the sample of Frew (2008) and Frew et al. (in preparation). Here, again we applied the calibration corrections detailed in Covey et al. (2007).

Name	D (kpc)	T_{eff} (kK)	u	g	r	i	*z*	Nebular contamination
Abell 13	1.6	113 ± 5	19.722 ± 0.038	19.601 ± 0.019	19.746 ± 0.015	19.734 ± 0.025	20.109 ± 0.120	Bright nebular rim in r
Abell 30	2.0	115 ± 5	14.051 ± 0.004	14.191 ± 0.010	15.221 ± 0.003	14.888 ± 0.004	15.042 ± 0.005	Faint
Abell 33	1.16	100 ± 5	15.213 ± 0.004	15.620 ± 0.003	16.116 ± 0.003	16.411 ± 0.004	16.857 ± 0.012	Faint
Abell 52	2.0	150 ± 20	17.514 ± 0.005	17.599 ± 0.006	17.722 ± 0.011	17.821 ± 0.008	17.936 ± 0.031	Very faint nebula in g
Abell 73	2.7	66 ± 10	22.151 ± 1.082	21.385 ± 0.042	20.906 ± 0.048	20.453 ± 0.045	20.196 ± 0.113	Faint nebula in all bands
BD+33 2642	3.1	20.2 ± 0.5	10.824 ± 0.001	10.635 ± 0.001	11.023 ± 0.001	11.360 ± 0.001	12.040 ± 0.003	Nebula unresolved
HDW 3	1.2	125 ± 5	16.770 ± 0.004	17.019 ± 0.005	17.263 ± 0.007	17.572 ± 0.007	17.767 ± 0.017	Very faint
IC 1747	2.6	74 ± 3	19.436 ± 0.064	16.851 ± 0.009	17.579 ± 0.006	19.052 ± 0.025	18.432 ± 0.045	Bright compact nebula in g and r
IRAS 21282+5050	2.4	20 ± 5	16.654 ± 0.003	15.161 ± 0.007	13.655 ± 0.008	13.408 ± 0.003	12.911 ± 0.004	Compact nebula with [WCL] CSPN
K 1-16	1.9	140 ± 5	14.183 ± 0.003	14.731 ± 0.004	15.282 ± 0.003	15.705 ± 0.004	16.101 ± 0.008	Nebula present in g
K 3-82	2.8	80 ± 5	21.734 ± 6.384	16.543 ± 0.006	16.196 ± 0.006	16.208 ± 0.009	15.278 ± 0.013	Nebula present in g
KLW 10	3.1	80 ± 5	19.717 ± 0.014	19.798 ± 0.020	19.821 ± 0.043	19.987 ± 0.035	20.144 ± 0.177	Very faint
Kn 31	3.1	80 ± 5	21.080 ± 0.115	20.552 ± 0.025	20.097 ± 0.027	19.874 ± 0.028	19.746 ± 0.090	Very faint
Kn 34	2.8	80 ± 5	21.629 ± 0.046	21.089 ± 0.056	20.867 ± 0.204	20.847 ± 0.087	21.851 ± 0.633	Very faint
Kn 61	2.6	140 ± 20	17.621 ± 0.006	18.047 ± 0.008	18.485 ± 0.011	18.811 ± 0.014	19.052 ± 0.046	Faint
KUV 03459+0037	0.5	91 ± 3	15.106 ± 0.003	15.488 ± 0.004	15.913 ± 0.004	16.248 ± 0.004	16.533 ± 0.008	No nebula
LDu 1	2.6	80 ± 5	23.307 ± 0.052	21.388 ± 0.055	21.231 ± 1.951	21.284 ± 0.104	22.091 ± 1.318	Very faint
LoTr 5	0.50	100 ± 5	11.080 ± 0.001	13.279 ± 0.007	12.143 ± 0.009	12.817 ± 0.009	9.275 ± 0.001	Very faint
M 1-1	4.0:	38 ± 10	14.893 ± 0.003	14.159 ± 0.002	14.173 ± 0.002	15.297 ± 0.003	15.220 ± 0.016	Bright compact nebula in g and r
M 1-75	1.8	150 ± 25	18.234 ± 0.004	15.895 ± 0.010	13.965 ± 0.062	15.182 ± 0.005	13.818 ± 0.005	Bright rim in g and r
NGC 650-1	1.2	140 ± 5	16.823 ± 0.008	16.892 ± 0.005	17.220 ± 0.004	17.511 ± 0.007	17.697 ± 0.021	Bright nebula in all bands
NGC 6210	2.1	61 ± 3	10.786 ± 0.007	11.459 ± 0.001	10.250 ± 0.011	11.382 ± 0.008	11.185 ± 0.002	Very bright, compact nebula
NGC 6309	2.1	97 ± 6	13.943 ± 0.003	12.504 ± 0.002	12.833 ± 0.002	13.547 ± 0.002	13.129 ± 0.003	Bright nebula in g and r
NGC 6894	1.2	80 ± 5	18.232 ± 0.011	18.786 ± 0.012	18.649 ± 0.018	18.361 ± 0.011	18.601 ± 0.036	Bright rim in g and r
NGC 7008	1.0	96 ± 4	13.792 ± 0.003	13.694 ± 0.010	13.948 ± 0.003	14.738 ± 0.011	13.074 ± 0.004	Faint nebula in g
Sn 1	6.5	80 ± 5	13.856 ± 0.004	14.150 ± 0.002	13.551 ± 0.003	14.598 ± 0.003	14.628 ± 0.004	Bright compact nebula in g
Te 2	2.0	80 ± 5	21.442 ± 0.033	21.046 ± 0.041	20.924 ± 0.141	20.811 ± 0.058	21.594 ± 1.096	Very faint
TS 1	1.0	90 ± 5	17.178 ± 0.005	17.479 ± 0.006	17.652 ± 0.009	18.208 ± 0.010	18.429 ± 0.038	Bright compact nebula in g and r
We 2-5	2.3	80 ± 5	20.121 ± 0.021	20.286 ± 0.030	20.409 ± 0.051	20.504 ± 0.055	21.729 ± 1.221	Very faint
WPS 46	0.7:	80 ± 5	16.094 ± 0.003	16.440 ± 0.004	16.942 ± 0.006	17.314 ± 0.006	17.687 ± 0.016	No nebula
WPS 54	0.45	125 ± 10	14.342 ± 0.003	14.850 ± 0.003	15.467 ± 0.003	15.873 ± 0.004	16.232 ± 0.007	No nebula

For several objects, the photometry of the central star is likely contaminated by the surrounding nebula. Nebular contribution in the g band is expected due to the presence of the [O III] • 5007 line in the middle of the filter bandpass. Nebular contamination in the r band also happens due the presence of the strong H• and [N II] lines in the filter bandpass. However, these lines tend to be weaker than the [O III] line in PN. There is no way to correct simply for nebular contamination as it changes according to filters, nebular excitation

Table 16. g • z excess for CSPN included in the sample of Frew (2008).

Name	E(B • V)	(g • z)$_0$	• (g • z)	M_{z2}	Comp. spec. type
Abell 13	0.45 ± 0.02	• 1.50 ± 0.14	• 0.15 ± 0.14	–	–
Abell 33	0.08 ± 0.00	• 1.41 ± 0.02	• 0.06 ± 0.02	–	–
Abell 52	0.45 ± 0.01	• 1.34 ± 0.05	• 0.04 ± 0.05	>12.10	Later than M6V
Abell 73	1.07 ± 0.05	• 1.19 ± 0.23	0.12 ± 0.23	>9.63	Later than M4V
K 1-16	0.03 ± 0.00	• 1.44 ± 0.02	• 0.07 ± 0.02	–	–
K 3-82	0.95 ± 0.01	• 0.83 ± 0.03	0.48 ± 0.03	2.87 [3.00–2.75]	F2V [F3V–F1V]
KLW 10	0.43 ± 0.04	• 1.58 ± 0.23	• 0.28 ± 0.23	–	–
Kn 31	0.13 ± 0.01	• 1.28 ± 0.06	0.02 ± 0.06	>11.58	Later than M5V
Kn 61	0.15 ± 0.03	• 1.54 ± 0.15	• 0.23 ± 0.15	–	–
KUV 03459	0.14 ± 0.01	• 1.35 ± 0.02	• 0.05 ± 0.02	–	–
NGC 650-1	0.26 ± 0.01	• 1.39 ± 0.03	• 0.02 ± 0.03	>12.33	Later than M6V
NGC 6309	0.25 ± 0.00	• 1.18 ± 0.01	0.16 ± 0.01	2.96 [3.08–2.85]	F3V [F4V–F2V]
NGC 6894	0.73 ± 0.02	• 1.42 ± 0.08	• 0.12 ± 0.08	–	–
NGC 7008	0.33 ± 0.01	• 0.11 ± 0.04	1.24 ± 0.04	5.02 [5.11–4.94]	G8V [G9V–G8V]
WPS 46	0.06 ± 0.01	• 1.38 ± 0.03	• 0.07 ± 0.03	–	–
WPS 54	0.00 ± 0.06	• 1.38 ± 0.24	• 0.08 ± 0.24	>7.93	Later than M2V

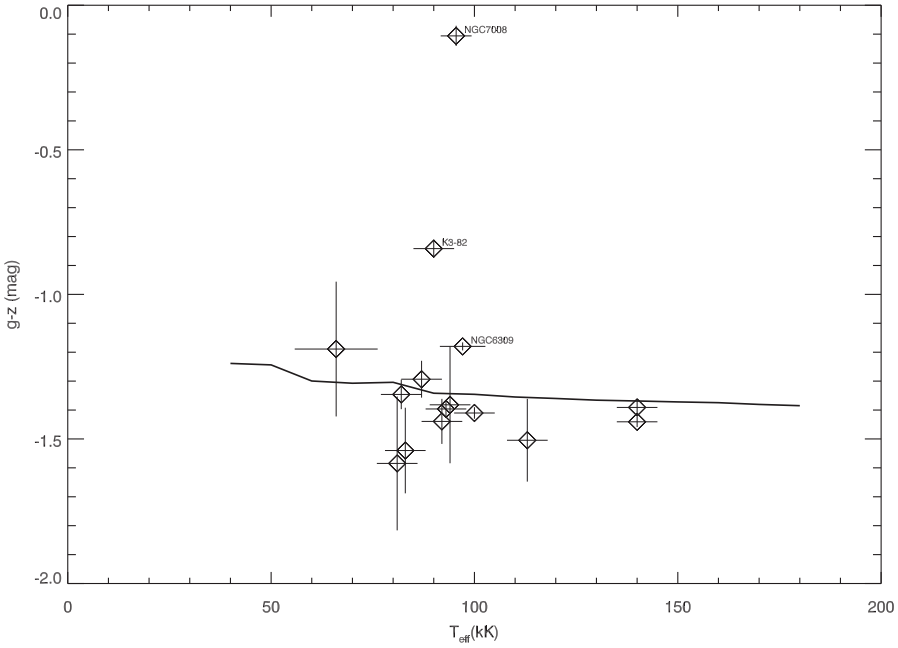

Figure 7. Predicted (solid line) versus observed (symbols) g • z colours as a function of stellar temperatures for the DR7 SDSS CSPNe. The CSPNe with an assumed temperature of 100 kK have been shifted in this figure between 80 and 100 kK for clarity. All symbols whose position below the line is not justified by the error bar are 'red deficit' objects caused by nebular contamination (see text). Such a high number of 'red deficit' objects highlights the importance of target selection and therefore the difficulty of using archival data for estimating the binary fraction of CSPNe.

class and nebular morphology. Therefore, we exclude here objects with a strong nebular contamination, either because the nebula is bright, or because it is compact, or both. This is the case for M 1-1, M 1-75, Sn 1 and TS 1 (listed in Table 15, but not 16).

For some objects the magnitudes are not consistent from one filter to another, indicating some flaw in the photometry that could be due to nebular contamination (IC 1747) or an erratic value from the SDSS photometry (Abell 30, the r band is not in line with other values). Some objects are either too bright or too faint to consider using their SDSS photometric measurements: the central stars BD+33 2642 and that in the middle of PN NGC 6210 are saturated, while the ones in A 73, Kn 34, LDu 1, Teutsch 2 and We 2-5 are too faint to provide adequate precision on the flux measurements. These faint central star tend to have a 'red deficit' justified by large error bars. Only A 73, despite its faintness, has an acceptably low error bar and we have left it in the result table (Table 16).

IRAS 21282+5050 is an object in transition between the asymptotic giant branch (AGB) and the PN phase and no information can be extracted from its colours due to nebular contamination and the dust surrounding this new PN. It is also a hydrogen-deficient star with characteristics similar to the late [WC] CSPN (De Marco et al. 2002).

This quick analysis confirms that the use of surveys to look for new binaries is not straightforward. The photometric precision of SDSS observations is intrinsically sufficient for the quality of data we are looking for. The calibration of the SDSS photometry is also very good, with only a slight systematic effect when compared to our

I-band work. However, if an unvetted sample is considered, in which bright nebulae are common then, as expected, the survey becomes non-viable for our analysis. This naturally reduces considerably the number of PNe that can be used for our statistical purpose. One could remeasure the photometry from the SDSS raw images, but the effort is probably not justified since a reasonable subtraction of bright PN light can seldom be achieved.

Although we do not use this sample for statistical purposes, we flag five objects with colours consistent with single star colours: A 52, A 73, Kn 31, NGC 650-1 (also known as M 76, this CSPN is surrounded by a bright extended nebula) and WPS 54 (also known as PG0948+534, the SuperCosmos images[3] reveal an asymmetric diffuse feature in blue and red bands, so contamination from the nebula cannot be excluded). Two of these objects could have been made bluer by PN contamination, and their lack of an excess could therefore be due to that. These five CSPNe, along with the three for which an excess was detected (discussed below) should all be re-observed.

6.2.1 NGC 6309

The central star of this quadrupolar, high-excitation PN (Vázquez et al. 2008) shows an excess corresponding to an F3V companion. Bilíková et al. (2012) could not discern the CSPN from the nebula in the Spitzer Space Telescope IRAC bands. The SDSS images for this PN show that the nebula is as bright as the central star, implying serious nebular contamination in the photometry of the central star. Although this is a strong 16σ detection, it is possible that the PN only could create such a photometric artefact.

6.2.2 LoTr 5

This system is composed of an O-type subdwarf (150 000 K; Feibelman & Kaler 1983) and a chromospherically active, fast rotating ($v\sin i = 60\,\mathrm{km\,s^{-1}}$) G5III companion (5230 K; Jasniewicz et al. 1996). Van Winckel et al. (2014) have recently monitored the radial velocity of the barium-enhanced G5 giant, finding slow variation consistent with a binary orbital period of a few years. Thus, LoTr 5 represents another newly discovered system of intermediate period. This agrees with Jasniewicz et al. (1996) who first suggested that LoTr 5 is a wide binary in which accretion from the AGB wind induces the fast rotation of the giant (Montez et al. 2010). Montez et al. (2010) indicate that there is evidence that the X-ray emission observed at the system position is due to coronal activity associated with the rapidly rotating companion.

Our grid of cool star colours has been designed for main-sequence companion and is not suitable for giants. Furthermore, the CSPN is very bright and is saturated for this object. A quick look at the object's magnitudes shows that it gets brighter in the redder bands (especially in z), although no spectral type can be determined in this study.

6.2.3 NGC 7008

The central star of this PN has been resolved by the Hubble Space Telescope into a detached binary. Ciardullo et al. (1999) find a K3 companion if the object is placed at 0.4 kpc, implying a separation of 160 au. Using their distance and a temperature of 95.5k ± 3.8 K (Phillips 2003), we find a 31σ detection for a G8V companion. The difference in spectral types can be explained by the calibration shift of the SDSS photometry and slight nebular contamination, given the nebula is visible – but not very bright – on the SDSS plates. However, Frew et al. (in preparation) find that the CSPN is likely to be a G8 subgiant rather than a main-sequence star. There is also an X-ray point source detected by the Chandra X-ray Observatory (Kastner & Montez 2012), which is coincident with the CSPN, possibly suggesting the presence of an active companion.

6.2.4 K 3-82

Little information is available about this object in the literature. As described above, we assumed a temperature of 80 kK and $\log g = 7$. Placed at 2.76 kpc (Frew 2008), it displays a 16σ z-excess revealing an F3 companion. Its round/elliptical PN shows mostly in the g band, but contamination is expected to be minimal, as the PN is faint on the SDSS images.

7 THE REVISED BINARY FRACTION

In this section, we calculate the fraction of CSPN with a detected I- and/or J-band excess for the entire sample. On the assumption that flux excess corresponds to a companion, we then calculate the fraction of companions that have been missed by our survey because of faintness. Finally, we compare the CSPN binary fraction determined in this way with a prediction based on the binary fraction of the progenitor main-sequence population. To carry out this prediction, we account for the fact that in our survey we only work with unresolved binaries, hence we exclude by design binaries with separations larger than our spatial detection limit. Since the main-sequence binary fraction includes binaries at all separations, an adjustment needs to be made to compare the CSPN binary fraction with the main sequence's.

7.1 The fraction of PN central stars with a detected I- and/or J-band excess

The goal of our study is to estimate the binary fraction of CSPN using a statistically reasonable sample size. In the I band, we have added 9 new objects to the sample of 25 objects analysed in Paper I (revised down from 27, because of the new identification of two mimics in that sample: EGB 1 and K 2-2, see Section 8 for more details). An additional six objects were analysed in this study, which were already included in Paper I (see Table 10). Out of the 15 objects analysed in the current study, we detected 4 CSPNe with an I-band excess, or a fraction of 27 per cent. This number is comparable to the fraction of ∼28 per cent (7/25) from Paper I (revised from 32 per cent or 8 objects out of 27). It is noticeable that two-independent observing runs, albeit carried out with the same telescope, yield similar fractions, considering that the analysis technique has been completely revised. The estimated binary fraction for the whole sample is 32 per cent, 11 detections out of 34 bona fide CSPNe.

In the J band, we find a fraction of 43 per cent (3/7), to be compared with the detected fraction of 56 per cent (5/9) from Paper I. For the whole sample of 16 CSPNe, 8 detections yield an observed fraction of 50 per cent. A higher fraction in the J band is expected compared to the I band because of the higher sensitivity of the J band to fainter companions. There may also be a small bias towards finding binaries because a companion adds J-band flux and may push the object over the detectability limit – this however is not expected to be a large effect.

[3] Hambly et al. (2001), images available at http://www-wfau.roe.ac.uk/sss/

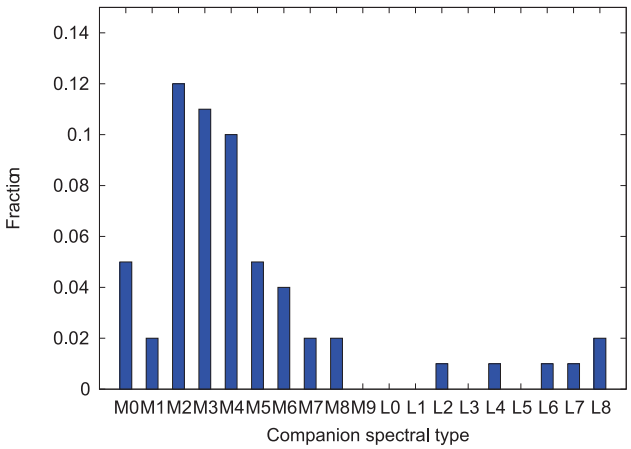

Figure 8. Spectral type distributions for the companions of main-sequence stars (Raghavan et al. 2010). The whole distribution is normalized to unity, but only spectral types later than M0V are plotted.

We estimate the error on our fractions using the normal approximation. Using the Wald interval to calculate a confidence interval, we find an error of 16 per cent in the I band and 24 per cent in the J band with a 95 per cent confidence level. The detected fraction of I-band excess is therefore 32 ± 16 per cent and of the J-band 50 ± 24 excess per cent.

7.2 Accounting for undetected companions

Faint companions cannot be observed with our technique. The brighter the central star the harder it becomes to observe its companion. To correct for completeness with respect to faint companions, we determine the companion spectral type detection limit of our entire survey by estimating the median of the upper limits for non-detections for the entire sample of 34 objects. In the I band, we find a median M4V spectral type limit, fainter than which, companions cannot be detected. In the J band, we find a similar median spectral type limit. The I-band limit is revised to slightly brighter than was obtained from the Paper I sample only, while for the J band it is revised to one to two spectral types brighter.

Using the normalized companion spectral type distribution of Raghavan et al. (2010) for main-sequence stars (see Fig. 8) we can account for undetected companions. Main-sequence binary systems with companions with a spectral type of M4V or brighter represent $80.^{+5}_{10}$ per cent of the main-sequence binary population. The error has been determined by taking the median absolute deviation of our sample of non-detections, yielding an uncertainty of one companion subtype in both the I and J bands. We correct the binary fraction for undetected companions and add this error to the one determined in Section 7.1. We find a binary fraction of 40 ± 23 per cent in the I band and 62 ± 49 per cent (where we have used an average error of 0.075 on the debiasing factor of 0.80 calculated above).

We note that changing the limiting spectral type for detection by as little as one spectral subtype changes the corrected fraction substantially. Hence, in Table 17, we put the number in parenthesis to emphasize its uncertain nature. To refine the debiased numbers, we will need a larger sample size so as to have a better idea of the spectral type limit of our survey.

Finally, degenerate companions are known to exist, but would not be detected by our survey, nor have we accounted for them when debasing for unobserved companions. Clearly, if we had, the binary fraction would be higher. Hillwig et al. (2010) suggest a quarter of a sample of 35 close CSPN binaries are such double degenerates, a number supported by the population synthesis considerations of Moe & De Marco (2012). If a quarter of all CSPN binaries had hot companions, then, considering that the CSPN binaries with main-sequence companions constitute 40–62 per cent of the entire population, we would have to add a further 13–21 points to account for the binaries with evolved companions.

Next, we estimate the fraction of CSPN binaries with separations larger than the limit imposed by our survey technique.

7.3 Comparison with the main-sequence binary fraction

Our targets are selected from the non-resolved binary pool. Once images are obtained with a particular setup, we double-check that none of the targets can be resolved into multiple sources by our detection algorithm. The algorithm will detect as two, sources that are farther apart than • 0.5 arcsec, or approximately one-third of our median seeing in photometric conditions. However, this number is estimated when both stars have the same luminosity, but varies as a function of the flux ratio of the observed couple of stars. We use a magnitude difference of 2 between the primary and its companion and look for the smallest separation between two resolved stars with such a flux ratio in our images, yielding a • 2 arcsec separation. We therefore use this number, equivalent to 1.4 times the median seeing of our observations, as the separation limit for binaries detected by our technique in the I band. Similarly for the J-band limit, we use 2.8 arcsec corresponding to 1.4 times the 2MASS resolution of 2 arcsec (Skrutskie et al. 2006). The values we used here are slightly higher than those used in Paper I because it was realized that a binary with such a flux ratio would be harder to resolve.

Table 17. The binary fraction of CSPN. The I and J band estimates should agree, and do within the error limits. The prediction from the main-sequence binary fraction should only agree with the observations if the entire main-sequence population (singles and binaries), except those close main-sequence binaries that go through a CE on the RGB, make a PN.

Prediction of the CSPN binary fraction	Fraction comp. brighter M4V a <2110 (I) or 2300 (J) au	Fraction all MS companions a <2110 (I) or 2300 (J) au	Fraction all MS companions all a
Using the I-band search	0.32 ± 0.16	(0.40 ± 0.20)[a]	(0.46 ± 0.23)[b]
Using the J-band search	0.50 ± 0.24	(0.62 ± 0.30)[a]	(0.71 ± 0.34)[b]
Using the main-sequence binaries	–	0.41 ± 0.03	0.47 ± 0.04

[a]If we were to add CSPN binaries with white dwarf companions, we would have to increase these fractions by 0.13 (I band) and 0.21 (J band), respectively (see Section 7.2).
[b]If we were to add CSPN binaries with white dwarf companions, we would have to increase these fractions by 0.15 (I band) and 0.24 (J band), respectively (see Section 7.3).

The median distance of our 34 targets is 0.95 kpc while for the 16 J-band subsample it is 0.74 kpc. As discussed in Paper I, using a de-projection factor of 0.9 to account for random phase, random orientation and the fact that eccentric systems spend more time at apastron, we obtain a corresponding median orbital separation of 2110 au in the I band and 2300 au in the J band. In other words, our I-band sample of 34 targets contains on average only binaries with a projected separation smaller than 2110 au (2300 au for the J-band sample) or else the binary would have been detected as resolved. Hence, to obtain the binary fraction at all separations one needs to add the binaries with separations larger than these limits.

Ultimately, we want to compare the PN binary fraction with that of the main-sequence progenitor population. Since the main-sequence binary fraction is for binaries at all separations we need to determine the fraction of those main-sequence binaries that evolve into central star binaries with separations larger than 2110 (or 2310) au. Since orbital separation increases because of mass-loss, the main-sequence binary separation will be smaller than these values. In Paper I, we had estimated that orbital separations for the CSPN binaries will be on average larger by a factor of ∼2.5 compared to the main-sequence binary population. In other words, an average central star binary with a separation of 2110 au (2300 au) had a separation of 844 au (921 au) while on the main sequence. We therefore scale the CSPN binary fraction up by adding the fraction of main-sequence binaries with separations larger than 844 au (921 au). Only then can we compare the CSPN binary fraction to the main-sequence binary fraction.

To evaluate the fraction of such wide main-sequence binaries, we convert the 844 au (921 au) limits into periods by using Kepler's third law and a system's mass of 1.5 $M_{\odot}$: log(P) = 7.0. We also need to be aware that main-sequence binaries with periods smaller than log P = 2.43 (5 per cent of all main-sequence stars; see Paper I) will go through a common envelope on the red giant branch (RGB), and never ascend the AGB, thereby eliminating themselves from the pool of binaries that become binary CSPN. Using a Gaussian fit of the main-sequence binary period distribution of Raghavan et al. (2010) and integrating under the curve between log P = 2.43 and 7.0, we discover that 78 per cent of all main-sequence binaries (or 39 per cent of all main-sequences stars, using a binary fraction of 50 per cent, see below) reside within those limits. The errors on these estimates are very small because of the logarithmic nature of the period limits.

The blue subsample (F6V–G2V) of the analysis of Raghavan et al. (2010), consistent with a 1.2 $M_{\odot}$ median mass progenitor of PN (Moe & De Marco 2006). The binary fraction of this subsample is 50 ± 4 per cent.[4] Hence of all the main-sequence stars that ascend the AGB (95 per cent of the total), 53 per cent (50/95) are single, 41 per cent (39/95) are binaries with separations smaller than 844 au (921 au) and the remaining 6 per cent are wider binaries. Multiplying the CSPN binary fractions with separations smaller than 2110 au (2310 au) by 1.15 ([41+6]/41), we obtain CSPN binary fractions at all separations of 46 ± 23 per cent for the I band and 71 ± 34 for the J band, where we have retained the relative errors. We list our debiased CSPN binary fractions for the I- and J-band analyses in Table 17 alongside the prediction from the main-sequence binary fraction (which is 41 per cent for the fraction with separations less than 844 or 912 au and 47 per cent for the fraction at all separations, once we have excluded those close main-sequence binaries that do not go up the AGB).

Finally, we note that if the double degenerate binaries really accounted for 25 per cent of the population, as we have discussed in Section 7.2, then the binary fraction determined here of 46–71 per cent (accounting for all main-sequence companions at all separations) should be increased by 13–21 points.

[4] This is the fraction of systems (where a system is a single or a multiple star), that are binaries, triples or higher order multiples.

8 NOTES ON INDIVIDUAL OBJECTS

8.1 A 28

This dim round nebula has also been discussed in Paper I. Including the data from that paper, we find no main-sequence companion brighter than M4V.

8.2 A 39

This canonical round nebula (Jacoby, Ferland & Korista 2001) is at a distance of 1.5 kpc (Danehkar et al. 2012). We find no main-sequence companion brighter than M3–4V. For this CSPN, we used the J magnitude from DR8 of the UKIDSS survey instead of the less accurate 2MASS J magnitude.

8.3 EGB 1

Multiwavelength images from the Wide-field Infrared Survey Explorer (Wright et al. 2010) show a bifurcated and irregular morphology which is unlike that expected for a PN. Combined with the arguments presented in Paper I, this indicates that EGB 1 is likely to be a mimic. Therefore, it has been removed from our sample.

8.4 EGB 6

This object has been discussed in Paper I. We used the magnitudes from Fulbright & Liebert (1993) yielding a more consistent H − K colour index. Since then, there has been the detailed study of Liebert et al. (2013) who provided fundamental data on the DAO primary star and its resolved companion, an M-type main-sequence star at a separation of 0.166 arcsec from the primary, equivalent to ∼96 au at a distance of 580 pc. At this distance, the I-band absolute magnitude from Liebert et al. (2013) suggests a companion type of M3V, earlier than our estimate of M5V from Paper I and this paper.

8.5 EGB 9

Ellis, Grayson & Bond (1984) noted this faint object from the Palomar Observatory Sky Survey Reid et al. 1991, suggesting it may be a very low surface brightness dwarf galaxy. Hoessel, Saha & Danielson (1988) took CCD images, suggesting it was more likely to be a diffuse nebula. It is seen on SHASSA Hα images of Gaustad et al. (2001) as an irregular elongated patch, indicating an emission rather than a reflection nebula. Narrow-band CCD images (though not reproduced in their paper) have been obtained by Kerber et al. (2000). It appears on our 2.1-m Hα+[N II] image to be a wisp of ionized interstellar medium (ISM), probably similar to the nebula around PHL 932 (Frew et al. 2010). We classified this object as a mimic. Frew (2008) noted the unusual colour of the putative ionizing star, which matches a mid-B star. As this is too cool to ionize the surrounding material, there must be an additional source of ionization present. Our method detected a G4 companion. As we have explained, when a bright, hot companion is present our method

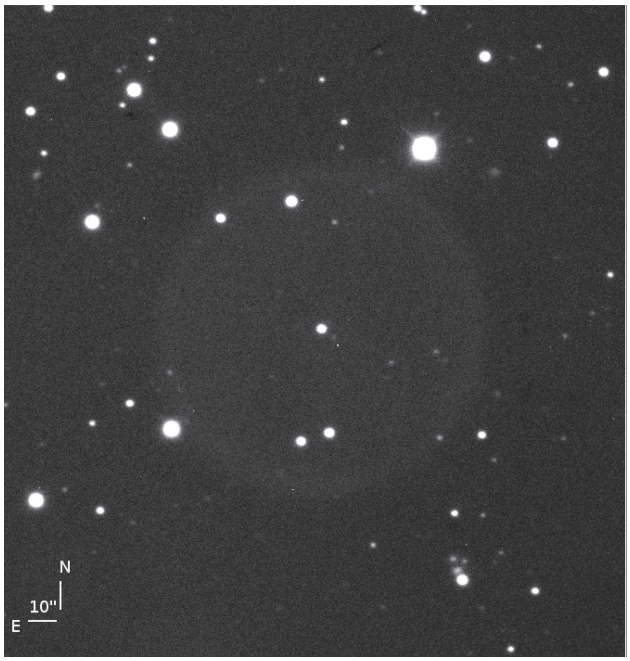

Figure 9. A 300 s exposure of the PN HaWe 10 in the V band showing this spherical nebula for the first time. The nebula has a radius of ∼110 arcsec.

will detect it, but the spectral type will not be reliable due to heavy contamination of all bands by the companion.

8.6 FP J1824-0319

This is the largest and closest PN discovered from the MASH survey (Parker et al. 2006), with an angular diameter of nearly 30 arcmin, and a distance of about 380 pc (Frew et al. 2013). Preliminary photometry of the CSPN was presented by Frew (2008) and is refined here. We find no clear I-band or J-band excess; using the latter, we estimate an upper limit of M4V for a main-sequence companion.

8.7 HaWe 10

This is a beautiful round PN similar to A 39 (Section 8.2) and Patchick 9 (Jacoby et al. 2010, see Fig. 9). We find no statistically significant NIR excess for the CSPN and impose a limit of M3V from I-band photometry.

8.8 Jacoby 1

This faint, round, high-excitation PN was discovered by Jacoby & van de Steene (1995). There have been several analyses of its hot hydrogen-deficient PG 1159 ionizing star published in the literature. We find no NIR excess, consistent with a companion spectral type later than M5V.

8.9 K 2-2

We have revisited the nature of this object here. Deep g' and r' images from DR 7 of the SDSS and r' and Hα images from the INT Photometric H-Alpha Survey (IPHAS; Drew et al. 2005) show that the observed nebula is seemingly connected to widespread diffuse material, suggesting the ionized ISM interpretation (see Paper I) is the more likely. Therefore, we have removed K 2-2 from our statistical analysis on central star binarity.

8.10 LTNF 1

We have confirmed this known close-binary CSPN (BE UMa; Ferguson et al. 1987, 1999; Ferguson & James 1994; Shimanskii et al. 2008) independently with our technique. The surrounding PN (Liebert et al. 1995) is extremely faint (log $S_{H\alpha} \simeq -6.3$) and our photometry is not affected by any problems of nebular contamination. However, our estimated spectral class of G5 disagrees with the temperature of the companion (4750 K) determined by Shimanskii et al. (2008) from detailed modelling of the system, which corresponds to a later spectral class of K3V. Shimanskii et al. (2008) also determined the companion mass to be only 0.25 $M_{\odot}$, which normally would indicate an M4 V companion. Thus, the companion is hotter and more luminous than its mass indicates, as is well known for strongly irradiated companions in close-binary systems (e.g. Exter et al. 2005; Wawrzyn et al. 2009). Although this system was known to be a close binary, it was selected for observations based on its V brightness and large, low surface brightness PN. As described in Section 2.1 and Paper I, this is the best way to obtain an unbiased binary fraction. When we recover a known binary, we also obtain an additional check of our technique. The discrepancy of the spectral types rests in the contamination of the spectral bands by the hot spot on the irradiated side of the companion.

8.11 Sh 2-68

The status of this nebula is uncertain, with two alternative hypotheses to explain its morphology and origin (Frew 2008). The extraordinarily detailed image taken with the 4-m Mayall Telescope at Kitt Peak[5] lends weight to the conclusions of Frew (2008), namely that this is probably an irregular, stratified H II region in the ambient ISM, despite the commentary provided on the NOAO web page. Owing to this ambiguity, we exclude Sh 2-68 from our statistical study. No companion was detected around this star to a limit of M4V.

8.12 Sh 2-216

This is the closest known PN to the Sun (Benedict et al. 2009). The central star has been recently studied by Rauch et al. (2007) and Gianninas et al. (2010). We do not have sufficient information to determine the presence of a companion to this CSPN, but we publish its U magnitude in Table 7.

8.13 SkAc 1

This little known nebula was discovered by Skiff and Acker (see Acker, Gorny & Cuisinier 1996) and independently as a candidate low surface brightness galaxy by Schombert et al. (1992) and Karachentseva, Karachentsev & Richter (1999), designated F 650-1 and KKR 4, respectively. It was reconfirmed as a PN by Makarov, Karachentsev & Burenkov (2003). As far as we know, no narrow-band image has been published in the literature, so we present our 2.1-m Hα image in Fig. 10. We detected an M4V companion around this CSPN with low confidence in the I band, but confirm the detection with much higher confidence in the J band.

[5] See http://www.noao.edu/image_gallery/html/im1164.html

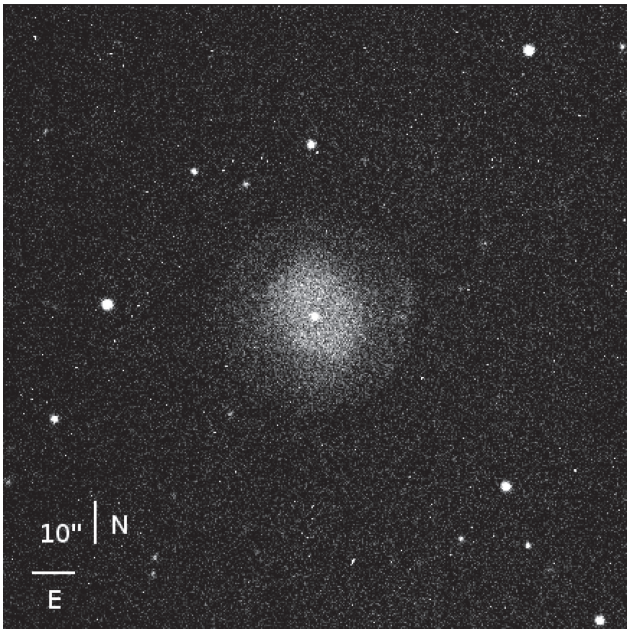

Figure 10. High contrast image of a 600 s exposure of the PN SkAc 1 in the [O III] filter from our observations.

Figure 11. IPHAS three colour (red = H•, green = R, blue = I) image of the nebula surrounding We 2-34. The image has been extracted from the Macquarie University GPN Database (Bojičić et al. 2011). The image is approximately 7 arcmin wide, north is towards the top, east towards the left.

8.14 We 2-34

This is a new binary CSPN. It has a very strong I- and J-band flux excess. The morphology of this faint nebula is either cylindrical or bipolar, viewed at modest inclination (Fig. 11).

9 SUMMARY AND DISCUSSION

In this work, we have continued the search for I- and J-band flux excess to detect cool companions around CSPN. We measured U, B, V and I-band fluxes of newly observed targets using PSF-fitting photometry. The aim of this paper has been to extend the sample analysed in Paper I, refine the technique and investigate the use of archival data.

To the Paper I sample of 25 objects (revised down from 27 because of the identification of two mimics) we add 9 new objects resulting in a sample of 34 objects in total. Of these 34 objects, 16 have also been observed in the J band and we analyse these data separately, as also done in Paper I. The detection rate in the combined samples in the I band is (32 ± 16) per cent, while in the J band it is (50 ± 24) per cent. The Paper I results are fully in line with the current analysis (the two fractions were 30 and 54 per cent, respectively). In addition, every detection and limit in the I band is consistent with the J band (within one to two spectral subtypes), as was also the case in Paper I.

The targets in common between Paper I and the current paper have consistent magnitudes. There may be a systematic effect between the two sets of a few hundreds of magnitude with Paper I magnitudes being slightly fainter, although this is not so in all common targets. Similarly, there may be a small systematic effect in that this work has slightly redder stars by one or two hundreds of a magnitude. This is very small and does not alter the conclusion on these objects. We therefore average all magnitudes which increase the accuracy of the estimate. None but one of the common targets (EGB 6) have a detected flux excess, but the limits have been slightly revised compared to Paper I to be generally more stringent by approximately one spectral subtype.

14 of our targets were observed by the SDSS. We carried out a z flux excess analysis using the g • r baseline to determine the reddening self-consistently. All detections and limits are recovered with good consistency, with the exception of a small systematic effect leading to companion spectral types and spectral type limits cooler by about one spectral subtype (and in some cases having colours slightly bluer than the single star limit).

In this paper, we have also analysed nebular contamination and its effect on colours. Typically, bright nebular light is not properly subtracted, usually because the nebula is too compact. This invariably leads to too high a reddening, thus reducing the red flux excess or even generating a 'red deficit', or a CSPN with a colour bluer than the single star limit. This is the reason why extending our analysis to any SDSS DR7 PN in common with the catalogue of Frew (2008) leads to many objects with red deficit and does not meaningfully increase the sample. This is why we only flag four possible binaries detected using SDSS data, as well as a handful of meaningful limits. These objects are not used for statistical purposes.

We have corrected the I- and J-band excess fractions to include faint, undetectable companions. We have calculated the companion brightness limit of our I- and J-band surveys to be M4V, by determining the median limit for each sample. We have used the companion spectral type distribution for main-sequence binaries of Raghavan et al. (2010) to obtain correction factors. Equivalent distributions are available for the white dwarf population (Farihi, Becklin & Zuckerman 2005; Debes et al. 2011) that are reasonably similar to the main-sequence companion distribution. However, the survey limit is close to the statistical mode of these distributions, making the exact distribution used a critical choice. For example, the white dwarf companion spectral type distribution peaks one or two subtypes cooler than for the main-sequence companion spectral type distribution. Consequently, using the WD companion

spectral type distributions to account for unobserved faint companions, yields CSPN binary fraction larger than what we present here. We decided to adopt the main-sequence companion distribution of Raghavan et al. (2010), to debias for unobserved companions as well as to account for separation biases, but note that correcting for unobserved companions is highly uncertain. We find corrected fractions of (40 ± 20) per cent in the I band and (62 ± 30) per cent in the J band. These fractions represent the CSPN binary fraction with separations smaller than 2110 and 2300 au, respectively. Comparing these numbers to those in Paper I (43–51 for the I band and 64–69 for the J band), we see they are at the lower range of those values. The reason is the different detection limits calculated for the non-detections, which have been slightly updated in this paper with a larger sample. A larger sample would argue for better limits, but we must remember that a shift of as little as one spectral subtype has a large effect on the derived fraction. We also note that we have not accounted for evolved, hot companions, which may constitute up to a quarter of all companions, increasing the binary fractions determined above by 13 and 21 points respectively.

To compare our CSPN binary fraction with that of the progenitor, main-sequence population of 50 ± 4 per cent, we need to reduce this value to 47 per cent, because 5 per cent of all main-sequence stars have companions so close that a common envelope phase will take place during the RGB. These objects do not continue on to the AGB ([50-5]/95 = 47). To finalize the comparison, we must add to the CSPN binaries those wide binaries not included in our survey, which are instead included in the main-sequence surveys (rightmost column in Table 17). Alternatively, we can take away from the main-sequence binary fraction the equivalent wide binaries (third column in Table 17). We note that the results of this work are very consistent with those of Paper I. However, here we have improved the determination of the separation bias which has reduced the completion factor from • 1.5 of Paper I to • 1.2 here. This is due to a smaller resolution limit used in Paper I, where the seeing was adopted, instead of using 1.4 times the seeing value, as more realistic to resolve our typical system, a primary and its companion with a difference in flux of 2 mag.

Nie, Wood & Nicholls (2012) have carried out a population synthesis study to predict the relative importance of different PN-producing evolutionary channels. Their study is distinct from those of others (e.g. Yungelson, Tutukov & Livio 1993; Han, Podsiadlowski & Eggleton 1995) in that they use the observed fraction of sequence E, Large Magellanic Cloud (LMC) binaries as calibration. The argument is that while various assumptions in population synthesis studies are prone to large uncertainties, the fact that • 1 per cent of all LMC giants in a given magnitude interval is comprised of close binaries, allows one to calibrate other more uncertain relations. From their table 1, we see that the binary fraction of PN (all binaries minus the single stars and those stars that have merged) is 77–95 per cent for their favourite model, or 72–84 per cent for a model with a lower exponent of the mass ratio distribution relation (their model 9), which is closer to what found by Raghavan et al. (2010). Our debiased fraction of 46–71 per cent is comparable, though on the lower side of their range. However, the comparison above may not be altogether fitting, in that the LMC has a younger stellar population than the Galaxy's, even considering only the Galactic thin disc. Because of this, one may expect that the binary fraction of main-sequence stars and of CSPN be larger there (Bouy 2011). On the other hand a younger, higher mass population could also mean the opposite, or a lower binary fraction in the PN population, if more massive stars readily blow a superwind unaided (i.e. when single; Moe & De Marco 2012).

It is undoubtedly difficult to reach a conclusion as to whether the binary fraction in CSPN points to binarity as a preferential channel in PN formation, the largest source of uncertainty at the moment being the still relatively small sample size and the determination of the brightness detection limit. The determination of a reliable, observationally derived binary fraction is a fundamental step on to which we can continue building our knowledge of the impact of companions on the lives of giant stars and the formation of PN. In this series of papers we aim, through the progressive accumulation of vetted data and the refinement of the analysis technique, to determine a reasonable estimate of such a number.

ACKNOWLEDGEMENTS

The authors thank the anonymous reviewer for his comments and suggestions. DD thanks Quentin Parker for his support during the writing of this paper and Ivan Bojičić for his help in using the Macquarie University GPN Database. OD acknowledges financial support from the Australian Research Council via the Future Fellowship scheme (FT120100452).

NOAO is operated by the Association of Universities for Research in Astronomy (AURA) under cooperative agreement with the National Science Foundation.

Funding for the SDSS and SDSS-II has been provided by the Alfred P. Sloan Foundation, the Participating Institutions, the National Science Foundation, the U.S. Department of Energy, the National Aeronautics and Space Administration, the Japanese Monbukagakusho, the Max Planck Society, and the Higher Education Funding Council for England. The SDSS website is http://www.sdss.org/. The SDSS is managed by the Astrophysical Research Consortium for the Participating Institutions. The Participating Institutions are the American Museum of Natural History, Astrophysical Institute Potsdam, University of Basel, University of Cambridge, Case Western Reserve University, University of Chicago, Drexel University, Fermilab, the Institute for Advanced Study, the Japan Participation Group, Johns Hopkins University, the Joint Institute for Nuclear Astrophysics, the Kavli Institute for Particle Astrophysics and Cosmology, the Korean Scientist Group, the Chinese Academy of Sciences (LAMOST), Los Alamos National Laboratory, the Max-Planck-Institute for Astronomy (MPIA), the Max-Planck-Institute for Astrophysics (MPA), New Mexico State University, Ohio State University, University of Pittsburgh, University of Portsmouth, Princeton University, the United States Naval Observatory, and the University of Washington.

REFERENCES

Abazajian K. N. et al., 2009, ApJS, 182, 543
Acker A., Gorny S. K., Cuisinier F., 1996, A&A, 305, 944
Ali A., Sabin L., Snaid S., Basurah H. M., 2012, A&A, 541, A98
Allen D. A., 1973, The Observatory, 93, 28
Benedict G. F. et al., 2009, AJ, 138, 1969
Bilíková J., Chu Y.-H., Gruendl R. A., Su K. Y. L., De Marco O., 2012, ApJS, 200, 3
Bojičić I. S., Parker Q. A., Filipović M. D., Frew D. J., 2011, MNRAS, 412, 223
Bond H. E., 2000, in Kastner J. H., Soker N., Rappaport S., eds, ASP Conf. Ser. Vol. 199, Asymmetrical Planetary Nebulae II: From Origins to Microstructures. Astron. Soc. Pac., San Francisco, p. 115
Bouy H., 2011, in Alves J., Elmegreen B. G., Girart J. M., Trimble V., eds, Proc. IAU Symp. 270, Computational Star Formation. Cambridge Univ. Press, Cambridge, p. 41
Cardelli J. A., Clayton G. C., Mathis J. S., 1989, ApJ, 345, 245

Ciardullo R., Bond H. E., Sipior M. S., Fullton L. K., Zhang C.-Y., Schaefer K. G., 1999, AJ, 118, 488
Covey K. R. et al., 2007, AJ, 134, 2398
Danehkar A., Frew D. J., Parker Q. A., De Marco O., 2012, in Manchado A., Stanghellini L., Schönberner D., eds, Proc. IAU Symp. 283, Planetary Nebulae: An Eye to the Future. Cambridge Univ. Press, Cambridge, p. 340
De Marco O., 2009, PASP, 121, 316
De Marco O., Clayton G. C., Herwig F., Pollacco D. L., Clark J. S., Kilkenny D., 2002, AJ, 123, 3387
De Marco O., Wortel S., Bond H. E., Harmer D., 2007, in Corradi R. L. M., Manchado A., Soker N., eds, Asymmetrical Planetary Nebulae IV. I.A.C. Electronic Publication, Spain, p. 529
De Marco O., Passy J.-C., Frew D. J., Moe M., Jacoby G. H., 2013, MNRAS, 428, 2118 (Paper I)
Debes J. H., Hoard D. W., Wachter S., Leisawitz D. T., Cohen M., 2011, ApJS, 197, 38
Drew J. E. et al., 2005, MNRAS, 362, 753
Drew J. E. et al., 2014, MNRAS, 440, 2036
Ellis G. L., Grayson E. T., Bond H. E., 1984, PASP, 96, 283
Exter K., Barman T., Pollacco D., Pustynski V., Bell S., Pustylnik I., 2005, in Burderi L., Antonelli L. A., D'Antona F., di Salvo T., Israel G. L., Piersanti L., Tornambè A., Straniero O., eds, AIP Conf. Proc. Vol. 797, Interacting Binaries: Accretion, Evolution, and Outcomes. Am. Inst. Phys., New York, p. 561
Farihi J., Becklin E. E., Zuckerman B., 2005, ApJS, 161, 394
Feibelman W. A., 1987, PASP, 99, 270
Feibelman W. A., Bruhweiler F. C., 1989, ApJ, 347, 901
Feibelman W. A., Kaler J. B., 1983, ApJ, 269, 592
Ferguson D. H., James T. A., 1994, ApJS, 94, 723
Ferguson D. H., Liebert J., Cutri R., Green R. F., Willner S. P., Steiner J. E., Tokarz S., 1987, ApJ, 316, 399
Ferguson D. H., Liebert J., Haas S., Napiwotzki R., James T. A., 1999, ApJ, 518, 866
Frew D. J., 2008, PhD thesis, Macquarie University
Frew D. J., Parker Q. A., 2007, in Corradi R. L. M., Manchado A., Soker N., eds, APN IV Conf. Proc. Asymmetric Planetary Nebulae IV. I.A.C. Electronic Publication, Spain, p. 475
Frew D. J., Parker Q. A., 2010, Publ. Astron. Soc. Aust., 27, 129
Frew D. J., Madsen G. J., O'Toole S. J., Parker Q. A., 2010, PASA, 27, 203
Frew D. J., Bojičić I. S., Parker Q. A., 2013, MNRAS, 431, 2
Fulbright M. S., Liebert J., 1993, ApJ, 410, 275
Gabler R., Kudritzki R. P., Mendez R. H., 1991, A&A, 245, 587
Gaustad J. E., McCullough P. R., Rosing W., Van Buren D., 2001, PASP, 113, 1326
Gianninas A., Bergeron P., Dupuis J., Ruiz M. T., 2010, ApJ, 720, 581
Girven J., Gänsicke B. T., Steeghs D., Koester D., 2011, MNRAS, 417, 1210
Hambly N. C. et al., 2001, MNRAS, 326, 1279
Han Z., Podsiadlowski P., Eggleton P. P., 1995, MNRAS, 272, 800
Harrington J. P., Feibelman W. A., 1983, ApJ, 265, 258
Harris H. C. et al., 2007, AJ, 133, 631
Herald J. E., Bianchi L., 2011, MNRAS, 417, 2440
Hillwig T. C., Bond H. E., Afşar M., De Marco O., 2010, AJ, 140, 319
Hoessel J. G., Saha A., Danielson G. E., 1988, PASP, 100, 680
Jacoby G. H., van de Steene G., 1995, AJ, 110, 1285
Jacoby G. H., Ferland G. J., Korista K. T., 2001, ApJ, 560, 272
Jacoby G. H. et al., 2010, Publ. Astron. Soc. Aust., 27, 156
Jasniewicz G., Thevenin F., Monier R., Skiff B. A., 1996, A&A, 307, 200
Jones D. H. et al., 2009, MNRAS, 399, 683
Kaler J. B., 1983, ApJ, 264, 594
Karachentseva V. E., Karachentsev I. D., Richter G. M., 1999, A&AS, 135, 221
Kastner J. H., Montez J., 2012, AJ, 144, 58
Kerber F., Furlan E., Roth M., Galaz G., Chanamé J. C., 2000, PASP, 112, 542
Landolt A. U., 1992, AJ, 104, 340
Liebert J., Tweedy R. W., Napiwotzki R., Fulbright M. S., 1995, ApJ, 441, 424
Liebert J., Bond H. E., Dufour P., Ciardullo R., Meakes M. G., Renzini A., Gianninas A., 2013, ApJ, 769, L32
Makarov D. I., Karachentsev I. D., Burenkov A. N., 2003, A&A, 405, 951
Mendez R. H., Herrero A., Manchado A., 1990, A&A, 229, 152
Mendez R. H., Kudritzki R. P., Herrero A., 1992, A&A, 260, 329
Miszalski B., Acker A., Moffat A. F. J., Parker Q. A., Udalski A., 2009a, A&A, 496, 813
Miszalski B., Acker A., Parker Q. A., Moffat A. F. J., 2009b, A&A, 505, 249
Moe M., De Marco O., 2006, ApJ, 650, 916
Moe M., De Marco O., 2012, in Manchado A., Stanghellini L., Schönberner D., eds, Proc. IAU Symp. 283, Planetary Nebulae: An Eye to the Future. Cambridge Univ. Press, Cambridge, p. 111
Montez R., Jr, De Marco O., Kastner J. H., Chu Y.-H., 2010, ApJ, 721, 1820
Napiwotzki R., 1999, A&A, 350, 101
Nie J. D., Wood P. R., Nicholls C. P., 2012, MNRAS, 423, 2764
Otsuka M., Tajitsu A., 2013, ApJ, 778, 146
Otsuka M., Tamura S., Yadoumaru Y., Tajitsu A., 2003, PASP, 115, 67
Parker Q. A. et al., 2006, MNRAS, 373, 79
Pereyra M., Richer M. G., López J. A., 2013, ApJ, 771, 114
Phillips J. P., 2003, MNRAS, 344, 501
Phillips J. P., 2004, MNRAS, 353, 589
Raghavan D. et al., 2010, ApJS, 190, 1
Rauch T., Ziegler M., Werner K., Kruk J. W., Oliveira C. M., Vande Putte D., Mignani R. P., Kerber F., 2007, A&A, 470, 317
Reid I. N. et al., 1991, PASP, 103, 661
Sanduleak N., 1983, PASP, 95, 619
Schlafly E. F., Finkbeiner D. P., Schlegel D. J., Jurić M., Ivezić Ž., Gibson R. R., Knapp G. R., Weaver B. A., 2010, ApJ, 725, 1175
Schombert J. M., Bothun G. D., Schneider S. E., McGaugh S. S., 1992, AJ, 103, 1107
Schwarz H. E., Monteiro H., 2006, ApJ, 648, 430
Shimanskii V. V., Borisov N. V., Pozdnyakova S. A., Bikmaev I. F., Vlasyuk V. V., Sakhibullin N. A., Spiridonova O. I., 2008, Astron. Rep., 52, 558
Skrutskie M. F. et al., 2006, AJ, 131, 1163
Stetson P. B., 1987, PASP, 99, 191
Stetson P., 2000, in Murdin P., ed., Software: Stellar Photometry. IoP Publishing, Bristol
Van Winckel H., Jorissen A., Exter K., Raskin G., Prins S., Perez Padialla J., Merges F., Raskin G., 2014, A&A, 563, L10
Vázquez R., Miranda L. F., Olguín L., Ayala S., Torrelles J. M., Contreras M. E., Guillén P. F., 2008, A&A, 481, 107
Wawrzyn A. C., Barman T. S., Günther H. M., Hauschildt P. H., Exter K. M., 2009, A&A, 505, 227
Weidmann W. A., Gamen R., 2011, A&A, 526, A6
Wright E. L. et al., 2010, AJ, 140, 1868
Yungelson L. R., Tutukov A. V., Livio M., 1993, ApJ, 418, 794
Zuckerman B., Becklin E. E., McLean I. S., 1991, in Elston R., ed., ASP Conf. Ser. Vol. 14, Astrophysics with Infrared Arrays. Astron. Soc. Pac., San Francisco, p. 161
Zwitter T., Munari U., 1994, A&AS, 107, 503

APPENDIX A: LOGS OF THE OBSERVATIONS

We present the logs of our observations in Table A1.

Table A1. logs of observations taken in photometric conditions.

Name	RA	Dec.	UT of the observation	Filter	Exp times	Night	Name	RA	Dec.	UT of the observation	Filter	Exp times	Night	Name	RA	Dec.	UT of the observation	Filter	Exp times	Night
Sh 2-216	04 43 21.27	+46 42 05.8	2011-03-11 04:11:35.0	U	3	1	WDSH 1	05 59 24.87	+10 41 40.4	2011-03-14 04:39:56.0	U	60	4	We 2-34	07 00 28.40	+04 20 30.4	2011-03-16 05:31:35.0	V	300	6
Sh 2-216	04 43 21.27	+46 42 05.8	2011-03-11 04:14:16.0	B	3	1	WDSH 1	05 59 24.87	+10 41 40.4	2011-03-14 04:42:29.0	B	30	4	We 2-34	07 00 28.40	+04 20 30.4	2011-03-16 05:38:04.0	B	300	6
Sh 2-216	04 43 21.27	+46 42 05.8	2011-03-11 04:15:37.0	V	3	1	WDSH 1	05 59 24.87	+10 41 40.4	2011-03-14 04:45:53.0	B	60	4	We 2-34	07 00 28.40	+04 20 30.4	2011-03-16 05:44:27.0	I	360	6
Sh 2-216	04 43 21.27	+46 42 05.8	2011-03-11 04:17:17.0	I	3	1	WDSH 1	05 59 24.87	+10 41 40.4	2011-03-14 04:49:05.0	V	60	4	Kn 39	10 54 13.6	• 61 44 16	2011-03-16 06:01:19.0	V	360	6
We 2-34	07 00 28.40	+04 20 30.4	2011-03-11 05:01:49.0	B	60	1	WDSH 1	05 59 24.87	+10 41 40.4	2011-03-14 04:54:25.0	I	60	4	Kn 39	10 54 13.6	• 61 44 16	2011-03-16 06:10:09.0	V	360	6
We 2-34	07 00 28.40	+04 20 30.4	2011-03-11 05:06:03.0	B	120	1	A8	05 06 38.42	+39 08 08.6	2011-03-14 04:59:37.0	U	120	4	Kn 39	10 54 13.6	• 61 44 16	2011-03-16 06:24:18.0	I	300	6
We 2-34	07 00 28.40	+04 20 30.4	2011-03-11 05:09:07.0	V	120	1	A8	05 06 38.42	+39 08 08.6	2011-03-14 05:03:36.0	B	120	4	Kn 39	10 54 13.6	• 61 44 16	2011-03-16 06:32:20.0	I	300	6
We 2-34	07 00 28.40	+04 20 30.4	2011-03-11 05:12:14.0	V	120	1	A8	05 06 38.42	+39 08 08.6	2011-03-14 05:12:19.0	V	240	4	Kn 39	10 54 13.6	• 61 44 16	2011-03-16 06:38:56.0	B	300	6
We 2-34	07 00 28.40	+04 20 30.4	2011-03-11 05:16:09.0	I	300	1	A8	05 06 38.42	+39 08 08.6	2011-03-14 05:17:28.0	I	240	4	Kn 39	10 54 13.6	• 61 44 16	2011-03-16 06:44:42.0	B	300	6
We 2-34	07 00 28.40	+04 20 30.4	2011-03-11 05:22:17.0	I	300	1	Kn39	10 54 13.6	• 61 44 16	2011-03-14 05:34:20.0	B	120	4	JnEr 1	07 57 51.63	+53 25 17.0	2011-03-16 07:16:16.0	V	30	6
EGB 9	07 18 57.93	+07 22 23.2	2011-03-11 05:38:11.0	I	3	1	Kn39	10 54 13.6	• 61 44 16	2011-03-14 05:38:51.0	V	240	4	JnEr 1	07 57 51.63	+53 25 17.0	2011-03-16 07:18:56.0	B	30	6
EGB 9	07 18 57.93	+07 22 23.2	2011-03-11 05:40:22.0	V	3	1	Kn39	10 54 13.6	• 61 44 16	2011-03-14 05:45:10.0	B	240	4	JnEr 1	07 57 51.63	+53 25 17.0	2011-03-16 07:20:51.0	I	60	6
EGB 9	07 18 57.93	+07 22 23.2	2011-03-11 05:42:08.0	B	3	1	Kn39	10 54 13.6	• 61 44 16	2011-03-14 05:51:10.0	I	300	4	Ton 320	08 27 05.54	+31 30 08.8	2011-03-16 07:39:16.0	U	120	6
HaWe 10	07 55 11.31	+09 33 09.3	2011-03-11 06:37:13.0	V	300	1	Kn39	10 54 13.6	• 61 44 16	2011-03-14 05:57:40.0	I	300	4	Ton 320	08 27 05.54	+31 30 08.8	2011-03-16 07:42:48.0	I	60	6
HaWe 10	07 55 11.31	+09 33 09.3	2011-03-11 06:43:59.0	V	300	1	Kn39	10 54 13.6	• 61 44 16	2011-03-14 06:48:26.0	V	300	4	Ton 320	08 27 05.54	+31 30 08.8	2011-03-16 07:46:15.0	B	30	6
HaWe 10	07 55 11.31	+09 33 09.3	2011-03-11 06:51:35.0	B	300	1	SkAc1	14 16 21.95	+13 52 24.4	2011-03-14 09:25:45.0	V	120	4	Ton 320	08 27 05.54	+31 30 08.8	2011-03-16 07:48:06.0	V	30	6
HaWe 10	07 55 11.31	+09 33 09.3	2011-03-11 06:59:09.0	I	300	1	SkAc1	14 16 21.95	+13 52 24.4	2011-03-14 09:29:47.0	B	120	4	EGB 6	09 52 59.00	+13 44 34.5	2011-03-16 08:01:32.0	U	60	6
JnEr 1	07 57 51.63	+53 25 17.0	2011-03-11 07:18:07.0	U	30	1	SkAc1	14 16 21.95	+13 52 24.4	2011-03-14 09:33:32.0	I	240	4	EGB 6	09 52 59.00	+13 44 34.5	2011-03-16 08:04:58.0	I	30	6
JnEr 1	07 57 51.63	+53 25 17.0	2011-03-11 07:20:00.0	U	60	1	A 39	16 27 33.74	+27 54 33.4	2011-03-14 09:53:15.0	U	60	4	EGB 6	09 52 59.00	+13 44 34.5	2011-03-16 08:08:02.0	B	30	6
JnEr 1	07 57 51.63	+53 25 17.0	2011-03-11 07:22:35.0	I	20	1	A 39	16 27 33.74	+27 54 33.4	2011-03-14 09:56:18.0	I	20	4	EGB 6	09 52 59.00	+13 44 34.5	2011-03-16 08:09:33.0	V	30	6
JnEr 1	07 57 51.63	+53 25 17.0	2011-03-11 07:24:15.0	I	60	1	A 39	16 27 33.74	+27 54 33.4	2011-03-14 09:58:10.0	V	10	4	EGB 6	09 52 59.00	+13 44 34.5	2011-03-16 08:11:27.0	I	60	6
JnEr 1	07 57 51.63	+53 25 17.0	2011-03-11 07:26:42.0	B	30	1	A 39	16 27 33.74	+27 54 33.4	2011-03-14 09:59:33.0	B	10	4	IC 972	14 04 25.92	• 17 13 40.5	2011-03-16 08:55:05.0	V	20	6
JnEr 1	07 57 51.63	+53 25 17.0	2011-03-11 07:29:05.0	V	30	1	H4-1	12 59 27.77	+27 38 10.5	2011-03-14 11:12:34.0	B	30	4	IC 972	14 04 25.92	• 17 13 40.5	2011-03-16 09:00:13.0	V	60	6
Ton 320	08 27 05.54	+31 30 08.8	2011-03-11 07:42:57.0	U	5	1	H4-1	12 59 27.77	+27 38 10.5	2011-03-14 11:14:28.0	V	30	4	IC 972	14 04 25.92	• 17 13 40.5	2011-03-16 09:02:21.0	B	60	6
Ton 320	08 27 05.54	+31 30 08.8	2011-03-11 07:45:00.0	I	5	1	H4-1	12 59 27.77	+27 38 10.5	2011-03-14 11:16:52.0	I	60	4	IC 972	14 04 25.92	• 17 13 40.5	2011-03-16 09:05:16.0	I	120	6
Ton 320	08 27 05.54	+31 30 08.8	2011-03-11 07:46:41.0	B	5	1	IC4593	16 11 44.54	+12 04 17.1	2011-03-14 11:38:47.0	B	5	4	IC 972	14 04 25.92	• 17 13 40.5	2011-03-16 09:08:47.0	U	120	6
Ton 320	08 27 05.54	+31 30 08.8	2011-03-11 07:48:05.0	V	5	1	IC4593	16 11 44.54	+12 04 17.1	2011-03-14 11:40:21.0	V	5	4	NGC 3587	11 14 47.734	+55 01 08.50	2011-03-16 09:25:07.0	V	10	6
A28	08 41 35.57	+58 13 48.4	2011-03-11 08:06:34.0	U	5	1	IC4593	16 11 44.54	+12 04 17.1	2011-03-14 11:42:25.0	I	5	4	NGC 3587	11 14 47.734	+55 01 08.50	2011-03-16 09:26:42.0	B	10	6
A 28	08 41 35.57	+58 13 48.4	2011-03-11 08:07:56.0	U	15	1	Sh2-68	18 24 58.41	+00 51 35.9	2011-03-14 12:02:31.0	U	60	4	NGC 3587	11 14 47.734	+55 01 08.50	2011-03-16 09:28:52.0	I	20	6
A 28	08 41 35.57	+58 13 48.4	2011-03-11 08:10:35.0	I	15	1	Sh2-68	18 24 58.41	+00 51 35.9	2011-03-14 12:05:23.0	I	30	4	NGC 3587	11 14 47.734	+55 01 08.50	2011-03-16 09:30:59.0	U	30	6
A28	08 41 35.57	+58 13 48.4	2011-03-11 08:12:41.0	I	15	1	Sh2-68	18 24 58.41	+00 51 35.9	2011-03-14 12:07:35.0	V	10	4	A 39	16 27 33.74	+27 54 33.4	2011-03-16 09:57:17.0	V	10	6
A 28	08 41 35.57	+58 13 48.4	2011-03-11 08:14:47.0	B	15	1	Sh2-68	18 24 58.41	+00 51 35.9	2011-03-14 12:09:09.0	B	20	4	A 39	16 27 33.74	+27 54 33.4	2011-03-16 09:58:07.0	V	10	6
A28	08 41 35.57	+58 13 48.4	2011-03-11 08:16:14.0	V	15	1	FPJ1824	18 24 40.88	• 03 19 59.6	2011-03-14 12:18:29.0	B	3	4	A 39	16 27 33.74	+27 54 33.4	2011-03-16 09:58:58.0	V	10	6
EGB 6	09 52 59.00	+13 44 34.5	2011-03-11 08:26:35.0	U	5	1	FPJ1824	18 24 40.88	• 03 19 59.6	2011-03-14 12:19:39.0	V	3	4	A 39	16 27 33.74	+27 54 33.4	2011-03-16 10:01:15.0	B	20	6
EGB 6	09 52 59.00	+13 44 34.5	2011-03-11 08:27:57.0	U	15	1	FPJ1824	18 24 40.88	• 03 19 59.6	2011-03-14 12:21:35.0	I	7	4	A 39	16 27 33.74	+27 54 33.4	2011-03-16 10:04:07.0	I	20	6
EGB 6	09 52 59.00	+13 44 34.5	2011-03-11 08:29:01.0	U	15	1	Sh2-68	18 24 58.41	+00 51 35.9	2011-03-14 12:34:28.0	U	60	4	A 39	16 27 33.74	+27 54 33.4	2011-03-16 10:06:38.0	U	50	6
EGB 6	09 52 59.00	+13 44 34.5	2011-03-11 08:31:12.0	I	30	1	Sh2-68	18 24 58.41	+00 51 35.9	2011-03-14 12:37:04.0	I	30	4	IC 3568	12 33 06.83	+82 33 50.3	2011-03-16 10:20:37.0	V	5	6
EGB 6	09 52 59.00	+13 44 34.5	2011-03-11 08:32:51.0	I	30	1	NGC6781	19 18 28.09	+06 32 19.3	2011-03-14 12:48:42.0	B	5	4	IC 3568	12 33 06.83	+82 33 50.3	2011-03-16 10:22:09.0	B	5	6
EGB 6	09 52 59.00	+13 44 34.5	2011-03-11 08:34:01.0	I	30	1	NGC6781	19 18 28.09	+06 32 19.3	2011-03-14 12:51:49.0	U	15	4	IC 3568	12 33 06.83	+82 33 50.3	2011-03-16 10:25:07.0	I	5	6
EGB 6	09 52 59.00	+13 44 34.5	2011-03-11 08:36:18.0	B	30	1	NGC6781	19 18 28.09	+06 32 19.3	2011-03-14 12:53:47.0	U	30	4	IC 3568	12 33 06.83	+82 33 50.3	2011-03-16 10:27:31.0	U	10	6
EGB 6	09 52 59.00	+13 44 34.5	2011-03-11 08:37:52.0	V	30	1	NGC6781	19 18 28.09	+06 32 19.3	2011-03-14 12:55:54.0	B	30	4	SkAc1	14 16 21.95	+13 52 24.4	2011-03-16 10:51:05.0	V	240	6
M7	11 14 47.734	+55 01 08.50	2011-03-11 08:58:08.0	B	25	1	NGC6781	19 18 28.09	+06 32 19.3	2011-03-14 12:57:35.0	V	30	4	SkAc1	14 16 21.95	+13 52 24.4	2011-03-16 10:57:39.0	B	240	6
NGC 3587	11 14 47.734	+55 01 08.50	2011-03-11 08:59:31.0	V	25	1	NGC6781	19 18 28.09	+06 32 19.3	2011-03-14 12:59:28.0	I	45	4	SkAc1	14 16 21.95	+13 52 24.4	2011-03-16 11:03:06.0	I	240	6
NGC 3587	11 14 47.734	+55 01 08.50	2011-03-11 09:01:16.0	I	25	1	Jacoby 1	15 21 46.58	+52 22 04.1	2011-03-16 11:21:01.0	V	10	6							
NGC 3587	11 14 47.734	+55 01 08.50	2011-03-11 09:03:11.0	U	25	1	Jacoby 1	15 21 46.58	+52 22 04.1	2011-03-16 11:23:21.0	B	10	6							
LTNF 1	11 57 44.78	+48 56 18.7	2011-03-11 09:19:16.0	U	15	1	Jacoby 1	15 21 46.58	+52 22 04.1	2011-03-16 11:24:48.0	I	10	6							

Table A1 – continued

Name	RA	Dec.	UT of the observation	Filter	Exp times	Night	Name	RA	Dec.	UT of the observation	Filter	Exp times	Night
LTNF 1	11 57 44.78	+48 56 18.7	2011-03-11 09:21:11.0	U	15	1	Jacoby 1	15 21 46.58	+52 22 04.1	2011-03-16 11:27:37.0	U	20	6
LTNF 1	11 57 44.78	+48 56 18.7	2011-03-11 09:23:09.0	I	15	1	IC 4593	16 11 44.54	+12 04 17.1	2011-03-16 11:46:01.0	V	10	6
LTNF 1	11 57 44.78	+48 56 18.7	2011-03-11 09:24:52.0	B	15	1	IC 4593	16 11 44.54	+12 04 17.1	2011-03-16 11:47:36.0	V	5	6
LTNF 1	11 57 44.78	+48 56 18.7	2011-03-11 09:26:11.0	V	15	1	IC 4593	16 11 44.54	+12 04 17.1	2011-03-16 11:50:46.0	B	5	6
SkAc 1	14 16 21.95	+13 52 24.4	2011-03-11 09:44:31.0	I	30	1	IC 4593	16 11 44.54	+12 04 17.1	2011-03-16 11:53:21.0	I	5	6
SkAc 1	14 16 21.95	+13 52 24.4	2011-03-11 09:48:05.0	I	120	1	IC 4593	16 11 44.54	+12 04 17.1	2011-03-16 11:55:02.0	U	5	6
SkAc 1	14 16 21.95	+13 52 24.4	2011-03-11 09:51:41.0	B	120	1	IC 4593	16 11 44.54	+12 04 17.1	2011-03-16 11:56:09.0	U	5	6
SkAc 1	14 16 21.95	+13 52 24.4	2011-03-11 09:54:53.0	V	120	1	Sa 4-1	17 13 50.35	+49 16 11.0	2011-03-16 12:09:13.0	V	10	6
NGC 6058	16 04 26.55	+40 40 58.9	2011-03-11 11:04:42.0	I	3	1	Sa 4-1	17 13 50.35	+49 16 11.0	2011-03-16 12:10:32.0	B	10	6
NGC 6058	16 04 26.55	+40 40 58.9	2011-03-11 11:06:56.0	B	3	1	Sa 4-1	17 13 50.35	+49 16 11.0	2011-03-16 12:13:21.0	I	10	6
NGC 6058	16 04 26.55	+40 40 58.9	2011-03-11 11:08:29.0	B	3	1	Sa 4-1	17 13 50.35	+49 16 11.0	2011-03-16 12:15:10.0	U	20	6
NGC 6058	16 04 26.55	+40 40 58.9	2011-03-11 11:10:20.0	I	3	1	NGC 6058	16 04 26.55	+40 40 58.9	2011-03-16 12:27:51.0	V	5	6
Na 1	17 12 51.89	−03 15 59.69	2011-03-11 11:15:40.0	I	3	1	NGC 6058	16 04 26.55	+40 40 58.9	2011-03-16 12:28:57.0	B	5	6
Na 1	17 12 51.89	−03 15 59.69	2011-03-11 11:18:22.0	I	10	1	NGC 6058	16 04 26.55	+40 40 58.9	2011-03-16 12:30:15.0	I	5	6
Na 1	17 12 51.89	−03 15 59.69	2011-03-11 11:20:26.0	B	10	1	Na 1	17 12 51.89	−03 15 59.69	2011-03-16 12:39:20.0	V	5	6

APPENDIX B: PHOTOMETRIC MAGNITUDES FOR INDIVIDUAL EPOCHS

We present the individual photometric measurements for each object and each night in Table B1.

APPENDIX C: SDSS COLOURS FOR CSPN

In Table C1, we present predicted colours in the SDSS bands of single post-AGB stars using TMAP and TheoSSA models. A similar table was presented in Paper I for Johnson filters. The indices given here are in the AB magnitude system to follow the SDSS-calibration standards. The corrections described in Covey et al. (2007) have been applied to obtain these numbers.

APPENDIX D: EXCLUDED OBJECTS

We have observed CSPN according to the selection criteria described in Section 2.1. Five objects however were at the limits of our criteria and were observed anyway due to target availability constraints but their analysis revealed to be unsatisfactory, as perhaps should have been expected. Three PNe (H 4-1, Na 1 and Sa 4-1) out of these five are distant and not part of the volume-limited sample of Frew (2008). They are bright PNe; thus, the PN and the central star essentially form a point source that is then included when integrating the flux within the PSF profile. The three other objects (IC 3568, IC 4593 and IC 972) are all bright compact PNe affecting the photometry of the central star. All these objects – apart from IC 972 – showed a great sensitivity to photometric input-parameter values, artificially high E(B − V) values, and systematically displayed a 'red deficit' in our V − I temperature diagram, typical of objects displaying contamination at least in the Johnson V band by various nebular lines (notably the strong [O III] line) and inducing an erroneously high reddening. Their I-band magnitudes are given here for completeness. This band is less affected by nebular contamination. However, for all these objects the PN is still visible on the images.

D1 H 4-1

This is a low-metallicity PN that belongs to the Galactic halo (Otsuka et al. 2003). We note that the in the second epoch of observation the star dimmed by about 0.3 mag compared to the first epoch (see Table B1). Monitoring may therefore reveal it to be a short-period binary. We also note that Otsuka & Tajitsu (2013) concluded, based on the stellar and nebular abundances, that this star must have a binary progenitor.

D2 Na 1

Allen (1973) estimated a PN visual diameter of 10 arcsec. Kaler (1983) measured the integrated Hβ flux. The spectrum from Jones et al. (2009) indicates an optically thin PN of moderately high excitation.

D3 Sa 4-1

Discovered by Sanduleak (1983), this is an optically thin PN of moderate excitation. The hydrogen-rich CSPN has been analysed by Feibelman (1987) and Feibelman & Bruhweiler (1989). The

Table B1. Photometric magnitudes of each object and each observation epoch.

Object	Night	U	B	V	I
A 28	1	15.153 ± 0.009	16.273 ± 0.009	16.523 ± 0.007	16.836 ± 0.010
A 39	4	14.137 ± 0.007	15.310 ± 0.007	15.613 ± 0.006	15.935 ± 0.009
A 39	6	14.125 ± 0.004	15.317 ± 0.004	15.619 ± 0.004	15.925 ± 0.008
EGB 6	1	14.479 ± 0.008	15.688 ± 0.008	15.991 ± 0.007	16.331 ± 0.007
EGB 6	6	14.457 ± 0.005	15.691 ± 0.006	16.004 ± 0.008	16.323 ± 0.014
EGB 9	1	12.863 ± 0.009	13.062 ± 0.008	13.133 ± 0.009	13.037 ± 0.010
FP J1824-0319	4	–	14.601 ± 0.006	14.841 ± 0.004	15.159 ± 0.010
FP J1824-0319	6	–	14.755 ± 0.003	14.596 ± 0.006	15.120 ± 0.012
H 4-1	4	–	16.465 ± 0.068	15.384 ± 0.081	17.491 ± 0.046
H 4-1	6	15.971 ± 0.019	16.846 ± 0.040	15.701 ± 0.056	17.736 ± 0.080
HaWe 10	1	–	17.549 ± 0.008	17.888 ± 0.005	18.259 ± 0.009
IC 3568	6	11.336 ± 0.015	12.204 ± 0.055	12.249 ± 0.072	12.752 ± 0.028
IC 4593	4	–	–	–	11.119 ± 0.006
IC 4593	6	9.719 ± 0.004	–	–	–
IC 972	4	17.774 ± 0.012	18.110 ± 0.008	17.471 ± 0.007	17.359 ± 0.011
IC 972	6	17.761 ± 0.022	18.049 ± 0.013	17.446 ± 0.007	16.530 ± 0.008
Jacoby 1	4	13.963 ± 0.005	15.217 ± 0.008	15.610 ± 0.005	16.020 ± 0.010
JnEr 1	1	15.519 ± 0.008	16.759 ± 0.008	17.101 ± 0.007	17.484 ± 0.009
JnEr 1	6	–	16.742 ± 0.009	17.118 ± 0.010	17.494 ± 0.016
LTNF 1	1	14.610 ± 0.011	15.739 ± 0.007	15.746 ± 0.006	15.269 ± 0.008
Na 1	6	15.810 ± 0.036	16.310 ± 0.084	15.570 ± 0.102	15.879 ± 0.060
NGC 3587	1	14.137 ± 0.008	15.394 ± 0.009	15.764 ± 0.007	16.165 ± 0.010
NGC 3587	6	14.155 ± 0.005	15.388 ± 0.006	15.779 ± 0.006	16.159 ± 0.009
NGC 6058	6	–	13.452 ± 0.004	13.802 ± 0.004	14.169 ± 0.007
NGC 6781	4	16.243 ± 0.039	17.111 ± 0.021	16.880 ± 0.016	16.439 ± 0.029
Sa 4-1	6	12.249 ± 0.004	13.427 ± 0.004	13.721 ± 0.005	14.064 ± 0.006
Sh 2-216	1	11.228 ± 0.007	–	–	–
Sh 2-68	4	15.809 ± 0.007	16.639 ± 0.009	16.455 ± 0.008	16.159 ± 0.008
Sh 2-68	6	–	16.661 ± 0.014	16.451 ± 0.009	16.203 ± 0.016
SkAc 1	1	–	18.198 ± 0.008	18.480 ± 0.007	18.535 ± 0.014
SkAc 1	4	–	18.182 ± 0.008	18.504 ± 0.008	–
SkAc 1	6	–	18.196 ± 0.005	18.482 ± 0.006	18.590 ± 0.013
Ton 320	1	14.171 ± 0.010	15.371 ± 0.009	15.687 ± 0.008	16.073 ± 0.012
Ton 320	6	14.150 ± 0.005	15.355 ± 0.005	15.697 ± 0.005	16.035 ± 0.007
WDSH 1	1	–	–	–	17.428 ± 0.022
We 2-34	1	–	19.876 ± 0.023	19.833 ± 0.017	19.217 ± 0.015
We 2-34	6	–	19.881 ± 0.040	19.844 ± 0.042	–

object was first listed in the Palomar-Green Survey of hot blue stars, designated PG 1712+493. Zwitter & Munari (1994) confirmed its PN nature spectroscopically, and found a diameter of 10 arcsec. For the CSPN, they inferred V • I = • 0.17 from the slope of the stellar continuum.

D4 IC 3568

IC 3568 is the archetypal round, double-shell PN (Harrington & Feibelman 1983). The parameters of the CSPN were determined by Mendez, Kudritzki & Herrero (1992). Owing to contamination from this bright nebula ($\log S_{H\alpha} = \bullet$ 2.0 erg cms$^{\bullet\ 2}$ s$^{\bullet\ 1}$), photometry of the central star is difficult.

D5 IC 4593

This is another high surface brightness PN ($\log S_{H\alpha} = \bullet$ 1.7), leading to nebular contamination of the stellar photometry. The central star has been extensively studied (see De Marco et al. 2007; Herald & Bianchi 2011; Bilíková et al. 2012), and shows radial velocity variations now attributed to wind variability (Mendez, Herrero & Manchado 1990; De Marco et al. 2007).

D6 IC 972

The CSPN of this object is surrounded by a bright nebula contaminating the star photometry in all U, B, V and I bands. Pereyra, Richer & López (2013) report a nebular velocity of 20–25 km s$^{\bullet\ 1}$ for this highly evolved object. This object is the only rejected PN displaying a flux excess instead of a red deficit. The excess found when taking the photometric magnitudes at face value corresponds to a 2σ G8V companion in the I band and a 4σ G6V companion in the J band. Although the nebula is quite bright for this object (visually as bright as the other two IC objects of this study), it is doubtful that nebular contamination only can create the observed flux excess, notably because as opposed to the two other CSPN surrounded by a bright PN, IC 972 did not show much sensitivity to the photometry input parameters, indicating a reasonable nebular subtraction. Therefore, the CSPN of this object might very well be a binary. We flag this object for further observation to unravel the true binary nature of this object, for instance using photometric monitoring.

Table C1. Predicted colours in the SDSS bands of single post-AGB stars using TMAP and TheoSSA models.

T_{eff} (kK)	log g	u − g (mag)	g − r (mag)	r − i (mag)	i − z (mag)	Abundance
20 000	4.00	− 0.0236	−0.432	−0.338	−0.287	0.7408/0.2504
20 000	5.00	0.007	−0.430	−0.338	−0.298	0.7408/0.2504
30 000	4.00	− 0.325	−0.506	−0.383	−0.339	0.7408/0.2504
30 000	5.00	− 0.304	−0.506	−0.382	−0.344	0.7408/0.2504
30 000	8.00	− 0.344	−0.483	−0.371	−0.352	0.7120/0.2780
40 000	4.00	− 0.436	−0.506	−0.386	−0.355	0.7383/0.2495
40 000	5.00	− 0.445	−0.520	−0.394	−0.361	0.894/0.106
40 000	5.80	− 0.466	−0.522	−0.398	−0.365	0.7383/0.2495
40 000	6.00	− 0.446	−0.521	−0.396	−0.364	0.7383/0.1466
40 000	7.00	− 0.469	−0.532	−0.399	−0.368	0.7120/0.2780
40 000	8.00	− 0.483	−0.525	−0.395	−0.368	0.7120/0.2780
50 000	4.00	− 0.463	−0.515	−0.391	−0.361	0.7383/0.2495
50 000	5.00	− 0.475	−0.530	−0.397	−0.364	1/0
50 000	6.00	− 0.507	−0.536	−0.399	−0.366	0.7124/2.775
50 000	7.00	− 0.517	−0.537	−0.401	−0.369	0.7124/2.775
50 000	8.00	− 0.531	−0.525	−0.401	−0.371	0.700/0.300
60 000	5.00	− 0.515	−0.537	−0.404	−0.371	0.700/0.300
60 000	5.80	− 0.524	−0.539	−0.403	−0.371	0.7383/0.2495
60 000	6.00	− 0.530	−0.545	−0.404	−0.371	0.7124/0.2775
60 000	7.00	− 0.538	−0.545	−0.404	−0.372	0.7124/0.2775
60 000	8.00	− 0.546	−0.534	−0.405	−0.374	0.700/0.300
70 000	5.00	− 0.532	−0.546	−0.409	−0.375	0.700/0.300
70 000	6.00	− 0.544	−0.549	−0.406	−0.372	0.7124/0.2775
70 000	7.00	− 0.550	−0.550	−0.407	−0.374	0.7124/0.2775
70 000	8.00	− 0.560	−0.543	−0.409	−0.376	0.600/0.400
80 000	5.00	− 0.545	−0.553	−0.412	−0.377	0.700/0.300
80 000	6.00	− 0.557	−0.554	−0.412	−0.377	0.700/0.300
80 000	7.00	− 0.562	−0.556	−0.411	−0.377	0.7124/0.2775
80 000	8.00	− 0.569	−0.551	−0.413	−0.379	0.700/0.300
90 000	5.00	− 0.548	−0.552	−0.411	−0.376	0.700/0.300
90 000	6.00	− 0.568	−0.564	−0.415	−0.380	0.7124 / 0.2775
90 000	7.00	− 0.573	−0.563	−0.414	−0.380	0.7124 / 0.2775
90 000	8.00	− 0.579	−0.558	−0.417	−0.381	0.700/0.300
100 000	6.00	− 0.578	−0.570	−0.418	−0.382	0.7124/0.2775
100 000	7.00	− 0.583	−0.569	−0.418	−0.382	0.7124/0.2775
100 000	8.00	− 0.587	−0.565	−0.419	−0.382	0.700/0.300
110 000	6.00	− 0.582	−0.566	−0.417	−0.380	0.700/0.300
110 000	7.00	− 0.590	−0.573	−0.420	−0.383	0.7124/0.2775
110 000	8.00	− 0.593	−0.569	−0.421	−0.382	0.700/0.300
120 000	6.00	− 0.585	−0.568	−0.417	−0.380	0.700/0.300
120 000	7.00	− 0.595	−0.576	−0.421	−0.383	0.7124/0.2775
120 000	7.00	− 0.593	−0.570	−0.419	−0.381	0.700 / 0.3
120 000	7.50	− 0.595	−0.571	−0.420	−0.382	0.700/0.3
120 000	7.50	− 0.590	−0.570	−0.419	−0.381	0.900/0.1
130 000	6.00	− 0.588	−0.569	−0.418	−0.380	0.700/0.3
130 000	7.00	− 0.599	−0.578	−0.422	−0.384	0.7124/0.2775
130 000	8.00	− 0.600	−0.574	−0.422	−0.383	0.700/0.300
140 000	6.00	− 0.590	−0.570	−0.419	−0.381	0.700/0.300
140 000	7.00	− 0.601	−0.580	−0.422	−0.385	0.7124/0.2775
140 000	8.00	− 0.604	−0.576	−0.423	−0.383	0.600/0.400
150 000	6.00	− 0.595	−0.578	−0.421	−0.385	0.7124/0.2775
150 000	6.00	− 0.592	−0.571	−0.419	−0.381	0.700/0.300
150 000	7.00	− 0.603	−0.581	−0.422	−0.385	0.7124/0.2775
150 000	8.00	− 0.603	−0.577	−0.423	−0.383	0.800/0.200
160 000	6.00	− 0.593	−0.572	−0.419	−0.381	0.700/0.300
160 000	7.00	− 0.605	−0.582	−0.423	−0.385	0.7124/0.2775
160 000	8.00	− 0.606	−0.579	−0.424	−0.383	0.700/0.300
170 000	6.00	− 0.591	−0.573	−0.420	−0.382	0.800/0.200
170 000	7.00	− 0.607	−0.583	−0.424	−0.386	0.7124/0.2775
170 000	8.00	− 0.607	−0.580	−0.424	−0.383	0.700/0.300

This paper has been typeset from a TEX/LATEX file prepared by the author.